La	Ce	Pr	Nd	Pm	Sm	Eu	Gd	Tb	Dy	Ho	Er	Tm	Yb	Lu
57	58	59	60	61	62	63	64	65	66	67	68	69	70	71
Lanthanum	Cerium	Praseodymium	Neodymium	Promethium	Samarium	Europium	Gadolinium	Terbium	Dysprosium	Holmium	Erbium	Thulium	Ytterbium	Lutetium
138.91	140.12	140.91	144.24	(145)	150.36	151.96	157.25	158.93	162.50	164.93	167.26	168.93	173.05	173.05

PAPER
Senthil Kumar Kuppusamy *et al.*
Ligand-field symmetry and magneto-optical correlations in
a luminescent Dy(III) single-molecule magnet

Ligand-field symmetry and magneto-optical correlations in a luminescent Dy(III) single-molecule magnet

Senthil Kumar Kuppusamy, [ID] *[a] Christian Pachl, [ID] [b,c] Zhaoyang Jing,[b] Sagar Paul, [ID] [d] Benoît Heinrich, [ID] [e] Olaf Fuhr, [ID] [b,f] Svetlana Klyatskaya,[b] Wolfgang Wernsdorfer, [ID] [a,d] Annie K. Powell, [ID] [a,b,c] Karin Fink [ID] [b] and Mario Ruben [ID] [a,b,g]

The establishment of ligand field (LF) symmetry around lanthanoid (Ln(III)) centres is of paramount importance to understand factors that govern magnetization relaxation in single-molecule magnets (SMMs). We investigated a luminescent mononuclear Dy(III) compound [Dy(BA)$_4$] (pip) (**1**), where pip is a piperidinium cation and BA is a benzoylacetonate ligand. The stoichiometric compound exhibits zero-field SMM characteristics; quantum tunnelling of magnetization (QTM) dominates magnetization relaxation. In the diluted version of the compound (**1**@Y), the QTM is mitigated, and Raman and Orbach processes are involved in the relaxation. The effective energy barrier (U_{eff} = 53.61 cm^{-1}; H_{DC} = 0 Oe) estimated for magnetization relaxation is comparable with the LF splitting (ΔE = 57.2 cm^{-1}) between the ground and first excited Kramers doublets (KDs) determined from the $^4F_{9/2} \rightarrow {}^6H_{15/2}$ Dy(III)-based transition recorded at 2.4 K. By analysing the emission spectrum of the isostructural Eu(III) analogue as a spectroscopic probe for site symmetry, the LF symmetry around the Dy(III) centre is assigned as C_{2v}. The close proximity (178 cm^{-1}) of the triplet state of the ligand and the $^4F_{9/2}$ state of the Dy(III) facilitates back energy transfer, thereby rendering **1** emissive only at cryogenic temperatures. The predictive accuracy of the complete active space spin–orbit configuration interaction (CASOCI) method is benchmarked against the experimental emission profile. Overall, we propose a strategy to assign effective LF symmetry around Dy(III), establish magneto-optical correlations, and provide a comprehensive analysis of the emission process of **1**.

Introduction

Coordination compounds composed of trivalent lanthanoid cations (Ln(III)) feature magnetic[1–6] and luminescence[7–11] pro-

[a]*Institute of Quantum Materials and Technologies (IQMT), Karlsruhe Institute of Technology (KIT), Kaiserstraße 12, 76131 Karlsruhe, Germany.*
E-mail: senthil.kuppusamy2@kit.edu
[b]*Institute of Nanotechnology (INT), Karlsruhe Institute of Technology (KIT), Kaiserstraße 12, 76131 Karlsruhe, Germany*
[c]*Institute of Inorganic Chemistry (AOC), Karlsruhe Institute of Technology (KIT), Kaiserstraße 12, 76131 Karlsruhe, Germany*
[d]*Physikalisches Institut (PHI), Karlsruhe Institute of Technology (KIT), Kaiserstraße 12, 76131 Karlsruhe, Germany*
[e]*Institut de Physique et Chimie des Matériaux de Strasbourg (IPCMS), CNRS-Université de Strasbourg, Strasbourg, France*
[f]*Karlsruhe Nano Micro Facility (KNMFi), Karlsruhe Institute of Technology (KIT), Kaiserstraße 12, 76131 Karlsruhe, Germany*
[g]*Centre Européen de Sciences Quantiques (CESQ), Institut de Science et d'Ingénierie Supramoléculaires (ISIS), 8 allée Gaspard Monge, BP 70028, 67083 Strasbourg Cedex, France*

perties desirable for applications. From the magnetism point of view, Ln(III) compounds possessing spin-bearing ground states are likely to act as single-molecule magnets (SMMs) that show magnetic bistability and magnetic hysteresis at the molecular level,[12–16] caused by bistable magnetic orientations separated by an energy barrier.[17] Consequently, mono- and multi-nuclear Ln(III)-based SMMs are proposed for applications in information storage and quantum information processing (QIP),[18–22] see also this recent view point.[23] Among these compounds, Dy(III)-based ones are at the forefront due to their high propensity to show SMM characteristics. Judiciously designed Dy(III) compounds show high blocking temperatures (T_B) and spin reversal barriers (U_{eff}).[24–34]

From the optical side, the linewidths of the Ln(III)-based emissive inter-configurational f–f transitions are narrow as a consequence of the shielded nature of the 4f orbitals by the outer-lying 5s and 6p orbitals.[11,35–38] The narrow linewidths offer a pathway to experimentally estimate the ligand field (LF) splitting (ΔE) between m_J Stark sublevels associated with the ground and

excited state multiplets of Tb(III), Dy(III), Er(III), and Yb(III) SMMs from photoluminescence (PL) spectra.[7,39–44] In the case of Dy(III) compounds, the emission is dominated by the $^4F_{9/2} \rightarrow \, ^6H_{15/2}$ and $^4F_{9/2} \rightarrow \, ^6H_{13/2}$ transitions in the visible region. Other low-energy transitions in the visible ($^4F_{9/2} \rightarrow \, ^6H_{11/2}$) and NIR ($^4F_{9/2} \rightarrow \, ^6H_{9/2}$; $^4F_{9/2} \rightarrow \, ^6H_{7/2}$; $^4F_{9/2} \rightarrow \, ^6H_{5/2}$; $^4F_{9/2} \rightarrow \, ^6F_{9/2}$ and $^4F_{9/2} \rightarrow \, ^6H_{7/2}$) regions have also been observed.[45] Among the transitions, the $^4F_{9/2} \rightarrow \, ^6H_{15/2}$ transition, involving the $^6H_{15/2}$ ground state composed of m_J ($J = \pm 15/2$ to $\pm 1/2$, not necessarily in order) LF split Stark sublevels, is of importance when slow relaxation of magnetization in Dy(III)-based SMMs is considered. A well-resolved PL spectrum of a Dy(III) compound facilitates the estimation of ΔE between m_J Stark sublevels of the $^6H_{15/2}$ ground state multiplet. Additionally, the overall LF splitting energy of each state, for example $^6H_{15/2}$, can also be obtained from the PL spectrum, shedding light on the magnitude of the LF splitting, that is how much the ground and upper Stark levels are separated.[46]

In an ideal scenario, the magnetization relaxation in Dy(III) SMMs is expected to proceed *via* the upper Kramers doublet (KD8) of the $^6H_{15/2}$ ground multiplet and the energy barrier for spin-relaxation can be determined by estimating the energy difference between the ground KD1 and KD8.[47] However, this is often not the case, and there exist several spin-relaxation pathways that could bypass the ideal pathway. For example, the presence of phonon modes (collective lattice vibrations) could spur the spin-relaxation by presenting pseudo energy barriers, which lie below the first excited KD (KD2).[48,49] In such a scenario, the luminescence spectrum of Dy(III) compounds could serve as an ideal way to discern the ΔE values. For example, a smaller U_{eff} value, estimated from the relaxation time (τ) *versus* temperature (T) (Arrhenius-) plot, relative to the ΔE between the ground and first excited Stark levels obtained from the fine-structured luminescence spectrum is an indication of underbarrier spin-relaxation. Additionally, the magnitude of LF splitting (that is, the energy separation between the first and eighth Stark levels for $^6H_{15/2}$) estimated from PL studies could indicate the maximum U_{eff} value that could be obtained in an ideal scenario. In the case of the best SMMs showing high blocking temperatures (T_B) and U_{eff}, the magnitude of LF energy spread is above 1000 cm^{-1}. In hindsight, a relatively small magnitude of LF splitting, typically spanning several hundreds of cm^{-1}, estimated from PL studies already indicates a nominal SMM property.[45]

In the case of emission, the levels involved in the transitions are assigned assuming free-ion wavefunctions. And it is not possible to directly discern the exact wavefunction composition of Stark levels involved in transitions from the PL spectrum. In a similar vein, the exact composition of KDs and transition probabilities between them are not discerned from magnetic measurements. Transition probabilities between the KDs and the wavefunction composition of the KDs constituting the $^6H_{15/2}$ state, for example, can be obtained by performing computational studies. A comparison between the U_{eff} values obtained from the AC studies, LF splitting energies estimated from luminescence studies, and wavefunction compositions and transition probabilities between the KDs calculated by employing appropriate computational models provides a

detailed understanding of the magnetization relaxation process in Dy(III)-based SMMs. Moreover, experimentally determined ΔE values serve as an ideal benchmark to test the predictive accuracy of computational models, whose shortcomings such as basis set dependency and neglect of dynamic correlation are well-documented.

Beyond the magnitude of LF splitting and energy differences (ΔE) between Stark sublevels, the LF symmetry around Dy(III) plays a crucial role in governing the nature of magnetization relaxation in SMMs.[2,47] Continuous shape measure (CShM) analysis,[50] using the SHAPE programme, of the molecular structures obtained from single-crystal X-ray diffraction (SC-XRD) studies are commonly adopted to infer the coordination geometry around the Dy(III) centres. In the CShM analysis, positions of coordinating atoms around Dy(III) are considered and a geometry that shows minimal deviation from the ideal geometry is conceived as the coordination geometry. Such assignment has two shortcomings. First, molecular structures are commonly determined above 77 K, well above the temperatures at which AC measurements are performed. Any possible geometric rearrangements that could reflect on the magnetic properties are not captured by the CShM analysis. Second, a direct correlation between the SHAPE determined minimally distorted coordination environment around the Ln(III) ions and SMM properties is not ideal, considering the fact that SHAPE values reflect on geometric distortion based on the positional arrangement of atoms, not the effective LF and the actual electrostatic potential felt by the metal ion, see a recent discussion by V. R. M. Nielsen and T. J. Sørensen in this regard.[51] Such shortcomings mandate the need for alternative approaches to infer the effective LF symmetry around Dy(III) centres. A plausible solution to the issue is low-temperature photoluminescence studies of Eu(III) compounds that are isostructural to Dy(III) compounds. The f–f transitions constituting the Eu(III) emission are sharp, hypersensitive to the LF symmetry, and well-understood.[52–54] Such attributes render Eu(III) emission as a reliable spectroscopic probe for LF symmetry.[55–58] Consequently, a direct correlation between the LF symmetries between isostructural Eu(III) and Dy(III) compounds can be established.

The above discussion presents a plausible multi-technique pathway to elucidate structure–property relationships in Dy(III) SMMs. For such elucidations, a Dy(III) compound that features sharp and well-resolved emission lines and zero-field SMM characteristics is desirable.[59] Consequently, we prepared a mononuclear Dy(III) compound, [Dy(BA)$_4$](pip) (**1**), where pip and BA stand for the piperidinium cation and benzoylacetonate ligand, respectively. The compound was chosen for the following reasons. Firstly, the mono-nuclear Eu(III) compound [Eu(BA)$_4$](pip) (**2**)[8,60] is isostructural to compound **1**. Secondly, slow relaxation of magnetization is reported in tetrakis ligand coordinated compounds of the composition [Dy(L)$_4$](X), where X is a counter cation and L is a β-diketone ligand.[61–66]

We began by preparing compound **1** in its stoichiometric (Ln(III) = 100% Dy) form and studied its magnetic and photo-luminescence characteristics. One of the factors mediating spin-reversal in SMMs is the intermolecular dipolar
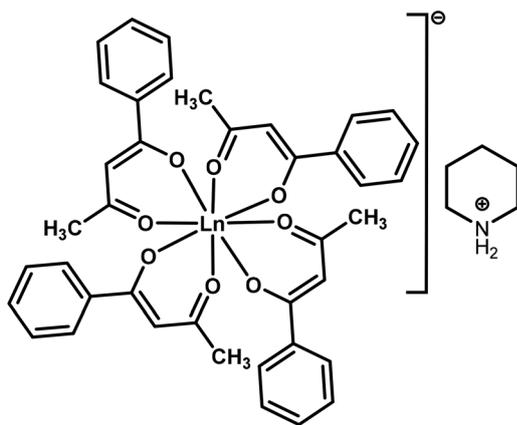
Ln = Dy (1), Eu (2), Dy:Y(2:98, 1@Y), or Gd (3)

Fig. 1 Molecular structure of Ln(III) compounds discussed in this study. Coordination of four benzoylacetonate ligands, each in bidentate fashion, with the central Ln(III) ion produces an eight coordinated anionic complex motif. The overall charge neutrality in the compounds is attained due to the presence of the piperidinium cation.

interaction.[3,47,67] By diluting an SMM entity in an isostructural Y(III)-compound matrix, intermolecular dipolar interactions contributing to the slow relaxation of magnetization could be mitigated. In order to do so, about 2% Dy(III)-doped isostructural Y(III) compound—$[Dy_{0.02}Y_{0.98}(BA)_4](pip)$, referred to as **1@Y**, is prepared. The triplet energy (E_T) of the BA ligand is estimated by preparing the isostructural Gd(III) compound (**3**) to shed light on the Dy(III) luminescence sensitization mechanism (Fig. 1).

In the following sections, we discuss on the magnetization relaxation processes in compounds **1** and **1@Y** and establish a correlation between the U_{eff} values derived from the AC studies and the LF splitting energies (ΔE) estimated from the PL studies. We interpret the effective LF around the Dy(III) centre in **1** by leveraging the emission properties of the isostructural Eu(III) compound **2**. Insights into mechanisms involved in the ligand sensitized luminescence from the Dy(III) centre as well as computational studies corroborating interpretations derived from the experimental studies are also presented.

Experimental and computational details

Direct current (DC), alternating current (AC), and field-dependent magnetization (*M versus H*) measurements

Gelatine capsules were used as sample holders at all the temperatures. Temperature-dependent DC susceptibility data were collected from 300 K to 2 K using a Quantum Design MPMS 3 SQUID magnetometer at an applied DC field of 1000 Oe. Diamagnetic corrections for the sample holder and eicosane were performed based on reference measurements. Intrinsic diamagnetic corrections for the stoichiometric and diluted ver-

sions of the compounds were employed using the relation: − (molecular weight/2) × 10^{-6} cm^3 mol^{-1}. Magnetic field *versus* magnetization data were collected from −7 T to 7 K using an MPMS-3 SQUID-VSM magnetometer (Quantum Design). For single quadrant *M versus H* and hysteresis measurements stable at each field, continuous sweep modes, respectively, were employed at a sweep rate of 30 Oe s^{-1}. Alternating current (AC) susceptibility measurements were performed at an AC field of 6 Oe.

Photoluminescence measurements

The studies were performed using a Fluorolog-QM-75-22-C all reflective spectrofluorometer. Data collection was performed using FeliX-FL software. A PowerArc energy efficient 75 watt "Green" ozone-free xenon illuminator with 64% lamp plasma collection efficiency emitting from 210 nm to the NIR was used as the light source. The following gratings were used: EX.: 300 nm–1200 l mm^{-1}, EM.: 400 nm–1200 l mm^{-1}. A cooled R928P PMT (185–900 nm) in TE-cooled housing was used to detect emission. A 400 nm long pass filter was used to cut second order diffraction peaks. Phosphorescence lifetime measurements were performed using a variable high repetition rate pulsed xenon source for excitation. Low-temperature and temperature-dependent PL measurements were performed using a Sumitomo closed cycle He cryostat. The ground crystalline samples were sandwiched between two quartz substrates and mounted on a cold finger. Emission data in the visible region are reported as corrected emission spectra accounting for instrument and optical artefacts. The steady state and lifetime data were plotted using Origin 2025b software. The estimation of CIE coordinates and Lorentz deconvolutions of the Dy(III)-based f–f transitions were performed using the CIE and peak deconvolution, respectively, apps in Origin 2025b. The lifetime data were fitted using a mono- or bi-exponential decay function included in the nonlinear curve fit module of Origin 2025b. Prior to the fitting, the data were normalized at the maximum intensity.

Additional experimental details are provided in the section S1 of the SI.

Complete active space spin orbit configuration interaction program (CASOCI) calculations

Starting from the molecular structure of **1** obtained from SC-XRD studies, the positions of the hydrogen atoms were optimized on a b3-lyp/def2-TZVP[68,69] level of theory using the rij approximation and by replacing Dy with diamagnetic Y using Turbomole 7.7.[70] To compute the magnetic properties, a multistep procedure was employed as outlined in the SI. Here, the energy was converged to $10^{-8}E_h$, the density was converged to 10^{-7} and scalar relativistic effects were considered on a DKH4 level of theory.[71,72] Afterwards, spin–orbit coupling was turned on by diagonalizing the full spin orbit coupled Hamiltonian in the active space (9 electrons in the 7 4f-orbitals) using our in-house developed *ab initio* Complete Active Space Spin Orbit Configuration Interaction Program

(CASOCI).[73] Lastly, using the same program, the obtained wavefunctions were analysed.

Results and discussion

Preparation and molecular structure of the Ln(III) compounds

The stoichiometric Dy(III) (**1**) and Gd(III) (**3**) and **1**@Y compounds are prepared (Scheme S1) in crystalline forms following a slightly modified method (see section S1) previously reported for the corresponding Eu(III) compound.[8] Crystallization of the Ln(III) compounds discussed in this study is promoted by seeding the mother liquor with a few pre-formed compound crystals; whereas, in the previous case the crystals are obtained from the mother liquor without seeding. Because compounds **1** (CCDC 2010809) and **3** (CCDC 2441051) are isostructural, only the structural details of compound **1** are presented as follows. The compound crystallizes in the centrosymmetric monoclinic space group $P2_1/n$ with $Z' = 1$, as inferred from the single-crystal X-ray diffraction (SC-XRD) studies performed at 180 K (Table S1). The unit cell is composed of four units ($Z = 4$), each containing one $[Dy(BA)_4]^-$ anion and one piperidinium counter-cation. The Dy(III) ion is eight coordinated by oxygen atoms from the four BA ligands and the average Dy–O bond length is 2.36 Å. In each compound unit, hydrogen bonding interactions between the hydrogen atoms of the piperidinium cation and oxygen atoms of the two benzoylacetonate ligands (Fig. 2a) are present. The coordination geometry around Dy(III) is best described as a distorted square antiprism (SAP, Fig. 2b); SHAPE analysis[74] gives a continuous shape measure of 0.139 relative to the ideal D_{4d} symmetry (Table S2). The coordination environment around Dy(III) is asymmetric, yielding Λ and Δ enantiomeric forms (Fig. 2c). The enantiomers are present in a

1 : 1 ratio and are related by inversion. Homochiral neighbours are connected by the 2_1 screw axis parallel to crystallographic axis b, whereas inversion links heterochiral Λ and Δ pairs. The packing therefore constitutes a racemic lattice with alternating inversion-related enantiomers and homochiral sequences propagated by the screw axis.

As shown in Fig. 2(b), O1, O2, O3, O4 and O5, O6, O7, O8 form two opposing square faces of a square antiprism. However, the edge lengths (a) of these two faces range from 2.75 Å to 2.91 Å, demonstrating considerable structural distortion. Furthermore, the distance (d) between the centers of the two faces is 2.52 Å. The ratio d/a_{avg} (where $a_{avg} = 2.83$ Å) is 0.890, which exceeds the d/a value of 0.841 in the ideal square antiprism. This indicates that the distorted square antiprismatic coordination geometry around the central dysprosium ion is axially elongated. A mean skew angle (Φ) of 42.64° and a mean magic angle (α) of 57.74° are deduced from the molecular structure of compound **1** (see Table S3). The deviations from the ideal values—$\Phi = 45°$ and $\alpha = 54.74°$—also indicate a distorted SAP LF geometry around the Dy(III) center. Further discussion on the LF geometry around the Dy(III) center and how the deviation from the ideal SAP geometry affects the magnetic and photoluminescence properties of **1** is presented in a later part of this manuscript.

For the characteristics of the molecular self-assembly, it should be noted that compound **1** forms a lamellar structure based on a rectangular in-plane arrangement of 4 molecules per lattice (area per molecule $A_{mol} = 92.5$ Å²) and a lamellar periodicity of one molecular layer $d_{lam} = 10.97$ Å (Fig. S1 and Table S4). The phase purity of the stoichiometric and diluted forms of the compound has been established by performing high-resolution powder X-ray diffraction (HR-PXRD) studies and indexing the powder patterns (Fig. S2 and Table S4). Powder patterns of com-
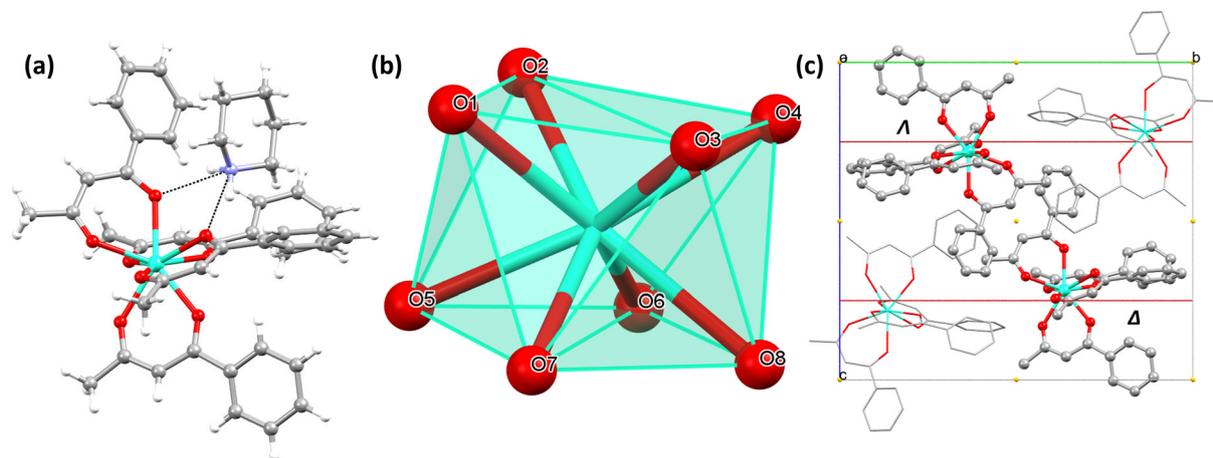

Fig. 2 Structure, coordination geometry, and unit cell packing of compound **1**. (a) Molecular structure of compound **1** obtained from the SC-XRD studies. Colour code: C, grey; Dy, teal; H, white; N, blue; O, red. The black dotted lines indicate hydrogen bonding interactions between two of the ligands and the counter cation. (b) Distorted SAP coordination geometry around Dy(III) in compound **1**. Magic (α) and skew (Φ) angles quantify the magnitude of distortion from an ideal SAP geometry. α and Φ represent the ligand–metal vector angle and the twist between square planes, respectively. A maximum of eight α and four Φ values are expected for a distorted SAP geometry. (c) Crystal packing of **1** viewed along the crystallographic c-axis, chosen to better visualize the enantiomers. The inversion related, yellow dots, Λ and Δ enantiomeric forms are shown as ball-and-stick models. The red lines indicate the screw axis relating homochiral fragments.

pounds **1** and **1@Y** are almost identical, except for small changes of intensity ratios due to the modification of electronic density contrasts following the substitution of Dy(III) by Y(III). The tiny changes in peak positions and lattice parameters between the powder and single-crystal forms of the compounds are explainable by the different temperatures at which the SC-XRD (180 K) and HR-PXRD (293 K) data are collected. From the HR-PXRD studies, the isostructural nature and phase purity of compounds **1** and **1@Y** are established.

We determined the Dy(III) content in **1@Y** using energy dispersive X-ray (EDX) spectroscopic studies (Section S3). The crystals were grown from a mother liquor prepared with a mixture of Dy(III) and Y(III) salts, which results in a random distribution of Dy(III) centres within the Y(III) lattice. This stochastic incorporation naturally leads to variations in the Dy(III) concentration across different crystallites (Fig. S3), reflecting on the measured Dy(III) concentrations of 2.1%, 1.9%, and 0% (Fig. S4–S6). The apparent 0% Dy(III) value can be rationalized by two factors: (i) detection sensitivity: in regions where Dy(III) incorporation is very low, the EDX signal may fall below the detection threshold, particularly when measured against the dominant Y(III) background. (ii) Crystallite size: the area analysed (Fig. S3, area 11) consisted of small crystallites, which further reduces the effective Dy(III) signal and can yield a negligible value. Thus, the reported values are interpreted as 2.1 ± 0.1% and 1.9 ± 0.1% considering the standard deviation of the values 2.1% and 1.9%.

Static and dynamic magnetic characteristics

Static magnetic characteristics of 1 and 1@Y. A χT value of 14.29 cm³ K mol⁻¹ (Fig. 3a) is obtained for the gently ground crystals of compound **1** at 300 K. The value is in the range (χT = 14.17 cm³ K mol⁻¹, J = 15/2, g = 4/3) expected for a mononuclear compound composed of one Dy(III) centre. χT = 14.29 cm³ K mol⁻¹ (300 K) is slightly higher than the expected spin-only value of 14.17 cm³ K mol⁻¹, corresponding to a difference of 0.84%. Such difference is ascribed to the combined uncertainties associated with the mass determination and diamagnetic correction. Cooling from 300 K resulted in a gradual decrease of the χT values. At 2 K, χT = 9.6 cm³ K mol⁻¹ was obtained. The decrease in the χT values at low temperatures is attributed to the depopulation of the excited crystal field split m_J sub-levels and the presence of magnetic anisotropy. Magnetization (M) versus Field (H) studies of the compound revealed an increase of the magnetization value until about 3.5 Tesla (Fig. 3b and S7). Subsequently, the magnetization gradually saturated, and at five Tesla M = 4.7 μ_B was obtained. This value is lower than the expected value of 5 μ_B for a single Dy(III) centre, attributed to the presence of significant magnetic anisotropy. Similar observations have been made for previously studied Dy(III) compounds composed of tetrakis β-diketonate ligands.[65]

For the **1@Y** compound, χT = 0.26 cm³ K mol⁻¹ at 300 K (Fig. S9a) and M = 0.097 μ_B (7 T) at 1.8 K (Fig. S9b) were obtained. By considering χT = 14.29 cm³ K mol⁻¹ obtained for **1** at 300 K, the Dy(III) content in the **1@Y** sample is estimated to be about 1.82%, comparable to the estimates obtained from the
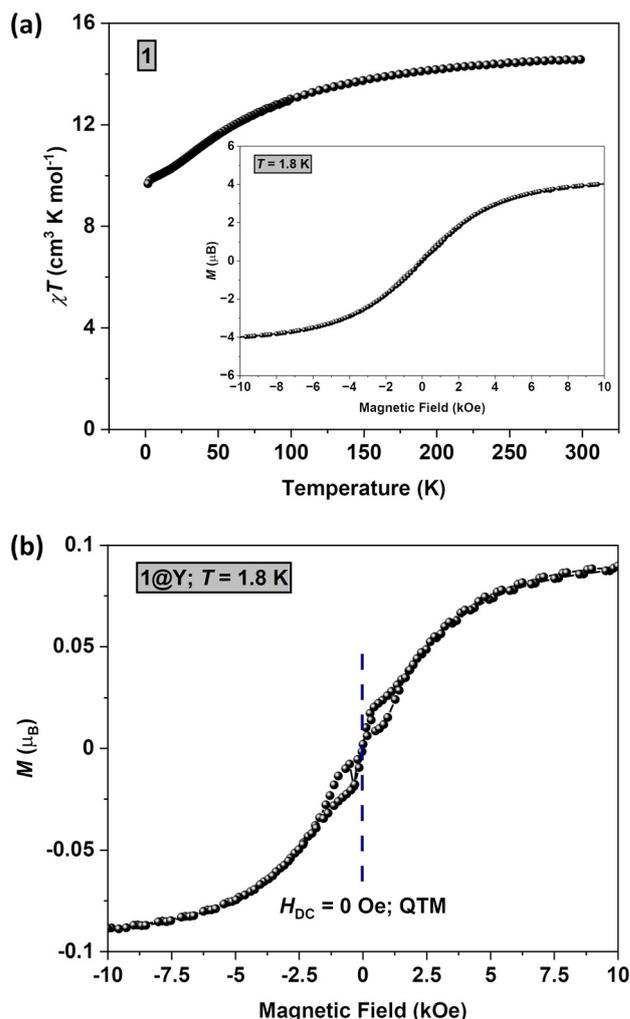

Fig. 3 (a) χT versus T plot of **1**. The inset shows the magnetization (M) versus field (H) plot of **1** obtained at 1.8 K. (b) $M(H)$ plot of **1@Y** at 1.8 K. The dashed blue line indicates quantum tunnelling of magnetization (QTM) at zero applied DC field (H_{DC} = 0 Oe). Additional temperature-dependent $M(H)$ plots of **1** and **1@Y** (in the −7 T to 7 T range) are presented in Fig. S7–S9.

EDX studies discussed above. Notably, a waist-restricted or butterfly-shaped hysteresis loop was observed for **1@Y** at 1.8 K (Fig. 3b) in the M versus H plot. To further investigate the static magnetization behaviour in the temperature range of 30 mK to 4.5 K, μ-SQUID measurements were performed on a single crystal of **1@Y** (Fig. 4). Characteristic waist-restricted or butterfly-shaped hysteresis loops are prominently observed in the sweep-rate-dependent $M(H)$ curves at 30 mK (Fig. 4a). Despite the pronounced zero-field quantum tunneling of magnetization (QTM) being evident, the loops remain slightly open up to about 2 K (Fig. 4b), in line with the $M(H)$ plot of **1@Y** at 1.8 K (Fig. 3b).

Dynamic magnetic characteristics of the stoichiometric and diluted compounds

Alternating current (AC) magnetic susceptibility study is an invaluable tool used to establish the SMM characteristics of a
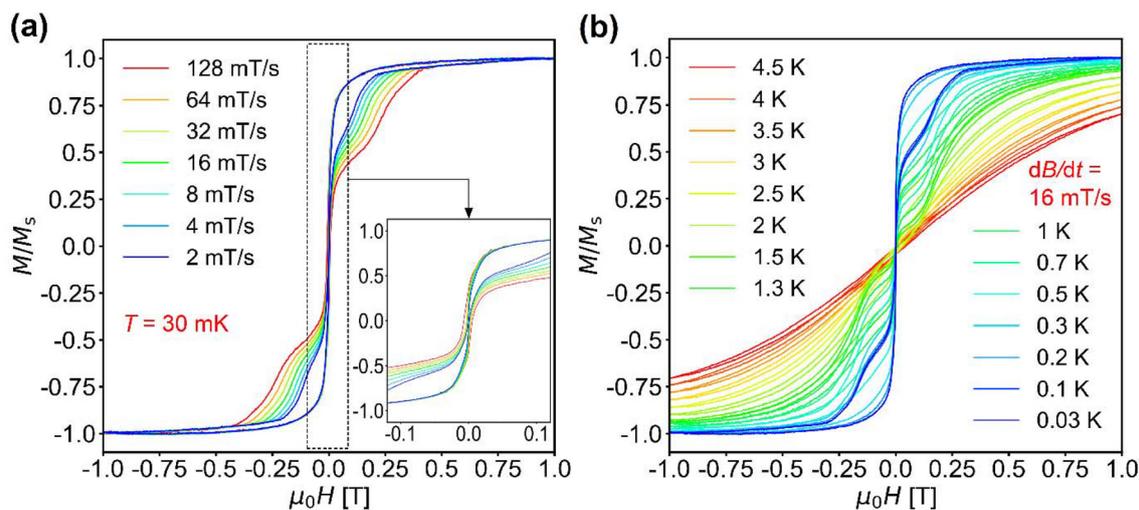
Fig. 4 (a and b) *M versus H* plots of **1**@Y obtained from the micro-SQUID (μ-SQUID) studies performed in the temperature range of 0.03 K to 4.5 K. The presence of magnetic hysteresis (see also Fig. 3b) indicates that the Dy(III) compound is an SMM.

compound. Information on the U_{eff} separating the two different spin orientations and mechanisms spurring the spin reversal between the orientations is obtained by fitting the relaxation time (τ) *versus* temperature (T) data collected from the AC studies. Frequency-dependent AC studies of compound **1** at 3 K in the absence of an applied DC field (H_{DC} = 0 Oe) revealed a peak in the out-of-phase susceptibility (χ'') component, indicating the zero-field SMM characteristics of the compound (Fig. S10). Applied DC-field-dependent studies in the 0 Oe to 2500 Oe range resulted in the shifting of the χ'' maxima to lower frequencies relative to the one observed at zero applied field until 1000 Oe. After that the χ'' maxima started shifting towards high frequencies. From the data shown in Fig. S10 and Table S5 and a field *versus* relaxation time (τ) plot shown in Fig. S11, an optimal DC field of 1000 Oe is inferred and temperature dependence of the magnetization relaxation studies has been studied at that field, to test the effect of applied magnetic field on the slow relaxation of magnetization of the compound.

Temperature-dependent AC studies of the compound showed χ'' peaks until 6 K at zero applied DC magnetic field (Fig. S12 and S13). By fitting the χ'' *versus* T data with the generalized Debye model, values of relaxation times (τ), isothermal (χ_T) and adiabatic (χ_S) magnetic susceptibilities, and distribution parameter (α) have been obtained (Table S6). The obtained α values indicate the distribution of relaxation times, attributed to the slight variation in the crystal field around the Dy(III) centers due to the presence of imperfections in the crystal lattice.

The modelling of the temperature *versus* lifetime data (Fig. 5a) can be satisfactorily performed using a combination of Raman (power law) and QTM processes (eqn (1)), see Table 1 for parameters obtained from the fitting.
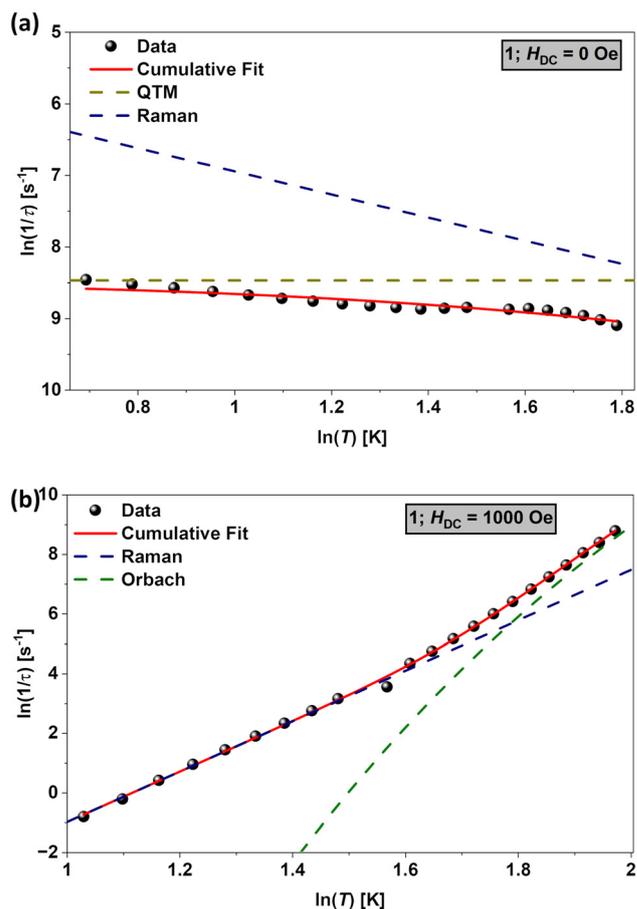
$$\tau^{-1} = \tau_{QTM}^{-1} + CT^n \qquad (1)$$

Fig. 5 Single-molecule magnetic characteristics of the stoichiometric Dy(III) compound (**1**). Relaxation time *versus* temperature plots of the compound at (a) H_{DC} = 0 Oe and (b) H_{DC} = 1000 Oe. The filled black circles are the experimental data points. The red lines are the cumulative fits obtained after modelling the data with appropriate combinations of relaxation processes (eqn (1) and (2)). The dashed lines are function plots showing individual mechanisms contributing to the magnetization relaxation.

Table 1 Parameters obtained from the modelling of the lifetime (τ) vs. T data of **1** and **1**@Y

Parameter	**1**		**1**@Y	
	H_{DC} = 0 Oe	H_{DC} = 1000 Oe	H_{DC} = 0 Oe	H_{DC} = 200 Oe
C (s^{-1} K^{-n})	205.82 ± 55.63	7.64 ± 1.95 × 10^{-5}	9.94 ± 2.71 × 10^{-4}	6.70 ± 0.71 × 10^{-5}
n	1.62 ± 0.17	8.47 ± 0.20	7.37 ± 0.22	8.91 ± 0.08
τ_0 (s)	2.1 × 10^{-4}	1.41 ± 1.26 × 10^{-10}	2.05 ± 0.77 × 10^{-9}	1.42 ± 0.46 × 10^{-10}
U_{eff} (K)	—	101.79 ± 6.27	77.13 ± 2.65	97.58 ± 2.25

where τ_{QTM}, C, and n are the rate of quantum tunnelling of magnetization, Raman coefficient, and Raman exponent, respectively. To get a satisfactory fit, we constrained τ_{QTM} using the experimental value of 1.61×10^{-4} s obtained from the isothermal $H(\tau)$ study (Table S5). From the fit, we obtained n = 1.62 ± 0.17, which is smaller than the n values in the range of 8–9 predicted for Kramer's ions such as Dy(III). However, n values smaller than the predicted values are regularly reported for Dy(III)-based SMMs and justified by invoking the contributions from low-energy acoustic phonons.[48,49] As shown in Fig. S12, the relaxation is dominated by QTM. Because the accessible AC measurement window for compound **1** is limited to 2 to 6 K, there is a strong overlap between QTM and Raman regimes, preventing an unambiguous separation of the individual relaxation processes. We propose this as the likely cause behind the small n value obtained for **1** at zero applied DC field, see also discussion below.

It is well-established that QTM can be suppressed, either completely or partially, by applying an external magnetic field. Such suppression is caused by the removal of energy degeneracy associated with the levels involved in the QTM process. In this context, the magnetization relaxation of compound **1** is studied under an optimal applied field of 1000 Oe. As shown in Fig. S14 and S15, χ'' peaks are observed at low frequencies, relative to the zero field measurements, when measurements were performed at 1000 Oe (Table S7). The observation indicates that the relaxation is slowed down by the external magnetic field. Modelling of the temperature versus relaxation time data obtained at 1000 Oe by employing eqn (2) revealed that the relaxation is caused by Orbach and Raman processes (Fig. 5b).

$$\tau^{-1} = CT^n + \tau_0^{-1} \cdot exp^{-U_{eff}/T} \tag{2}$$

where τ_0 and U_{eff} are the pre-exponential factor and effective energy barrier, respectively.

From the modelling we obtained U_{eff} = 101.79 ± 6.27 K (70.75 ± 4.36 cm^{-1}), see Table 1 for other parameters. Notably, the dominant QTM-mediated relaxation channel observed in the AC studies conducted at H_{DC} = 0 Oe is absent when the compound was studied under an applied field in the 2.8 K to 7.2 K temperature range.

It is well known that intermolecular dipolar interactions expedite the magnetization relaxation by enhancing the rate of QTM.[75] To mitigate the effect of dipolar interactions spurring the magnetization relaxation, compound **1** was diluted in the isostructural Y(III) compound matrix. Isothermal field versus susceptibility studies of **1**@Y revealed the presence of the χ'' peak at zero field; χ'' peak maxima are observed at smaller frequencies with applied fields (Fig. S16, S17 and Table S8). To study the effect of the applied field on the SMM properties, the AC data of **1**@Y were collected at zero and 200 Oe applied fields.

Dynamic magnetic susceptibility measurements of the **1**@Y compound in the absence of a DC field revealed χ'' peaks at much lower frequencies (Fig. S18–20) than the ones observed for the stoichiometric compound **1**. Moreover, upon increasing the temperature, the χ'' peaks shifted gradually to the high-frequency side, indicating a faster magnetization relaxation (Table S9). Such observation is in contrast to the one observed for compound **1** studied at zero applied DC field, where the χ'' maxima stayed almost constant upon temperature rise. Modelling of the lifetime versus temperature data, employing eqn (2), collected for **1**@Y under zero applied DC field revealed that the magnetization relaxation is induced by Raman and Orbach processes (Fig. 6a and Table 1). We obtain U_{eff} = 77.13 ± 2.64 K (53.61 ± 1.83 cm^{-1}) from the fitting.

The relaxation data (Fig. 6b) obtained from AC studies (Fig. S21, 22 and Table S10) of **1**@Y under the applied field of 200 Oe can also be fitted with eqn (2), indicating that the magnetization relaxation is induced by Raman and Orbach processes (Table 1). As expected, a higher U_{eff} is obtained for the compound under the applied field relative to the value obtained in the absence of a DC field.

We discuss two points before proceeding to the next section. Firstly, the Raman exponent (n = 1.62 ± 0.17) obtained for **1** at H_{DC} = 0 Oe is smaller than the values (in the range of 7.37 to 8.91) obtained for the compound at H_{DC} = 1000 Oe and for **1**@Y at H_{DC} = 0 Oe and 200 Oe. The QTM contribution is suppressed in the studied temperature range on application of a DC field and diamagnetic dilution, allowing the Raman relaxation channel to be more clearly resolved. Under these conditions, the extracted n values fall in the range (8–9) expected for a Kramers ion such as Dy(III). We attribute the increase in n with field and dilution to the progressive disentanglement of QTM and Raman processes, rather than a fundamental change in the Raman mechanism itself. We acknowledge that this attribution is tentative and subject to further verification.

Secondly, the waist-restricted hysteresis loop observed in the $M(H)$ study of **1**@Y at 1.8 K (Fig. 3b) signals the presence of QTM at low temperatures. This is further corroborated by the
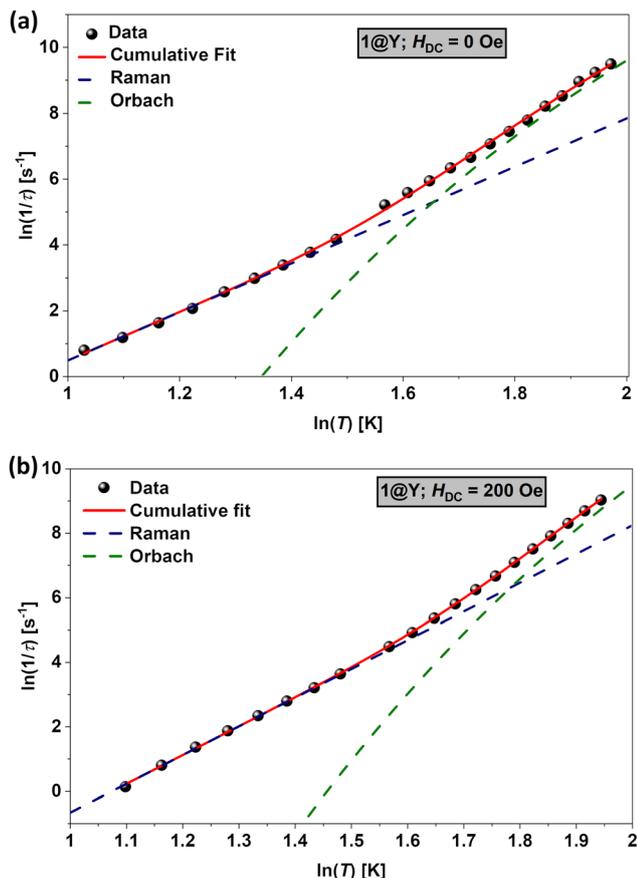
Fig. 6 SMM characteristics of **1**@Y compound. Relaxation time *versus* temperature plots of the diluted compound at (a) zero and (b) 200 Oe applied DC field. The filled black circles are the experimental data points. The red line is the cumulative fit obtained after modelling the data with Orbach and Raman relaxation processes. The dashed lines are function plots showing mechanisms (Orbach or Raman) contributing to the relaxation of magnetization.

Fig. 7 Corrected photoluminescence excitation (PLE) and photo-luminescence (PL) spectra of the stoichiometric Dy(III) compound (**1**). PLE and PL spectra of the compound at 2.4 K showing the $^4F_{9/2} \rightarrow {}^6H_J$ (J = 15/2, 13/2, 11/2, or 9/2) and $^4F_{9/2} \rightarrow {}^6F_{11/2}$ transitions in the 400 to 800 nm region. The PLE and PL spectra are obtained by monitoring the emission at 574 nm and exciting the sample at 359 nm, respectively. The following parameters are used to acquire the data: the excitation and emission slit widths are set to 7 mm and 0.2 mm, corresponding to spectral bandpasses of about 9.5 nm and 0.27 nm, respectively (Focal length = 700 mm). Step size 0.1 nm and integration time 0.1 s. A 400 nm long pass filter is used to exclude second order diffraction peaks.

$M(H)$ plots obtained from μ-SQUID measurements (Fig. 4). Upon dilution, the relaxation slows significantly, and the out-of-phase susceptibility (χ'') peaks become detectable only above 0.1 Hz (the lower limit of the magnetometer's frequency range) starting from 2.8 K. Consequently, QTM in **1**@Y could not be probed through AC susceptibility studies below 2.8 K. The residual QTM observed in diluted **1**@Y, after mitigation of intermolecular dipolar contributions, arises from intrinsic molecular parameters, most notably due to the distorted ligand field at Dy(III), as elaborated later in this study.

PL studies of compound 1

Well-resolved Dy(III)-based transitions—$^4F_{9/2} \rightarrow {}^6H_J$ (J = ±15/2, ±13/2, ±11/2, or ±9/2) and $^4F_{9/2} \rightarrow {}^6F_{11/2}$—in the visible and near infra-red (NIR) regions (Fig. 7) are observed for compound **1** at 2.4 K. Quantitative estimates of key photophysical parameters, such as excited-state lifetimes (Fig. S23 and 24), branching ratios (Tables S11 and S12), oscillator strengths (Table S12), and colour coordinates (Fig. S34–36 and Tables S13, S14), are presented in
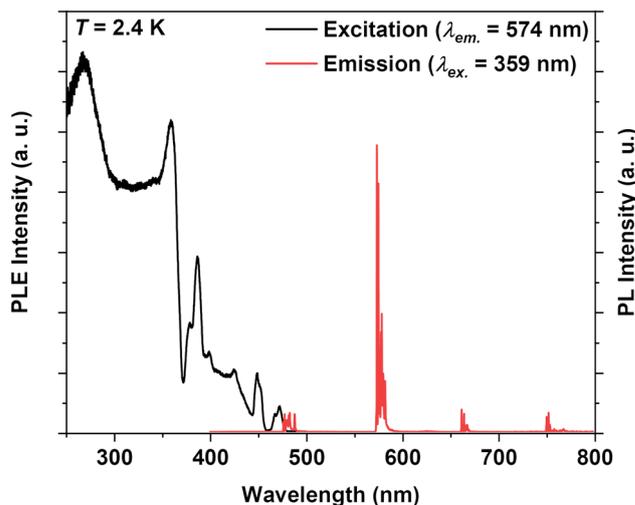
sections S5.1 to S5.4 of the SI. The Dy(III)-based emission is temperature- and excitation-wavelength-dependent (Fig. S25–33). The emission intensity progressively decreases with increasing temperature and at 300 K the compound is non-emissive. A discussion of the temperature-dependent emission behaviour and mechanistic factors responsible for this variation is provided in Section S5.5 (Fig. S37–S42) of the SI.

In the following, we examine the emission characteristics of compound **1** at 2.4 K to elucidate the LF splitting within the ^6H_J (J = 15/2, 13/2, 11/2, or 9/2) manifold. By exploiting the sensitivity of Eu(III) emission to local site symmetry,[76] we provide a comparative assignment of the effective LF at Dy(III) and elucidate a correlation between the magnetization relaxation and effective LF symmetry at Dy(III).

In order to assign the effective LF geometry around Dy(III) in **1**, we consider the emission characteristic of the isostructural Eu(III) compound (**2**; section S6)[8] because Eu(III) emission is a sensitive probe to the site symmetry.[55–58,77–83] In the emission spectrum of compound **2**, dominant $^5D_0 \rightarrow {}^7F_2$ and weak $^5D_0 \rightarrow {}^7F_0$ transitions (Fig. S43 and S44) are observed. The observation of the strong hypersensitive $^5D_0 \rightarrow {}^7F_2$ and $^5D_0 \rightarrow {}^7F_0$ transitions indicates that the ligand field symmetry around the Eu(III) is distorted from the SAP geometry featuring D_{4d} point group. Moreover, the observation of the $^5D_0 \rightarrow {}^7F_0$ transition, which is forbidden for D_{4d} point group, and removal of degeneracies of the $^5D_0 \rightarrow {}^7F_1$ and $^5D_0 \rightarrow {}^7F_2$ transitions indicate that the effective ligand field environment around the Eu(III) centre is best described as distorted SAP.

We have previously inferred C_{2v} point group symmetry for the Eu(III) compound by analysing the PL spectrum of the compound, in good agreement with a previous study,[84] see also Fig. 1.5 in this book chapter.[85] Considering the isostructural nature of the Eu(III) and Dy(III) compounds, see Table S3 for a comparison between the α and Φ values, and the comparable CShM values (Table S2), the above interpretation presented for the Eu(III) compound is also valid for the Dy(III) compound. That is, from the spectroscopic analysis of the compounds, the effective LF symmetry around Dy(III) is described as close to C_{2v} due to distortions from SAP geometry. The clear separation between the $^7F_0$ and $^7F_1$ levels, as observed in the emission spectrum of **2** shown in Fig. S43 and 44, allows the estimation of energy separation ($\Delta E_{0,1}$) between the levels from the PL spectrum. The estimated $\Delta E_{0,1} = 356.36$ cm^{-1} is comparable with $\lambda = 355.67$ cm^{-1}, λ is crystal field parameter as discussed in S6, obtained from the DC magnetic studies of compound **2** (section S6; Fig. S45). Such comparable estimates lend credibility to the assignment of distorted SAP LF geometry in the

Eu(III) compound by excluding contamination from the excited ^5D_J manifold and intermolecular magnetic interactions. See discussion in section S6.

To determine the overall crystal field splitting and energy separation between the m_J states of the ground ($^6H_{15/2}$) and excited states (^6H_J, $J = 13/2$, 11/2, or 9/2), the spectral data were deconvoluted by employing Lorentzian functions, see Fig. S46–49.[83,86] Eight Lorentzian functions satisfactorily reproduced the experimental data (Fig. 8a) in the 475 nm to 490 nm region corresponding to the $^4F_{9/2} \rightarrow {}^6H_{15/2}$ transition. The overall crystal field splitting of the $^6H_{15/2}$ state is 503.2 cm^{-1}. An energy separation of 57.2 cm^{-1} is estimated between the ground and first excited KDs (Table 2).

The $^4F_{9/2} \rightarrow {}^6H_{13/2}$ and $^4F_{9/2} \rightarrow {}^6H_{11/2}$ transitions can be satisfactorily deconvoluted using seven (Fig. 8b) and six (Fig. 8c) Lorentzian functions, respectively. Two sets of transitions are observed in the 745 nm to 775 nm spectral region, where the $^4F_{9/2} \rightarrow {}^6H_{9/2}$ transition is expected. The ones in the 745 nm to 760 nm range can be satisfactorily reproduced with five
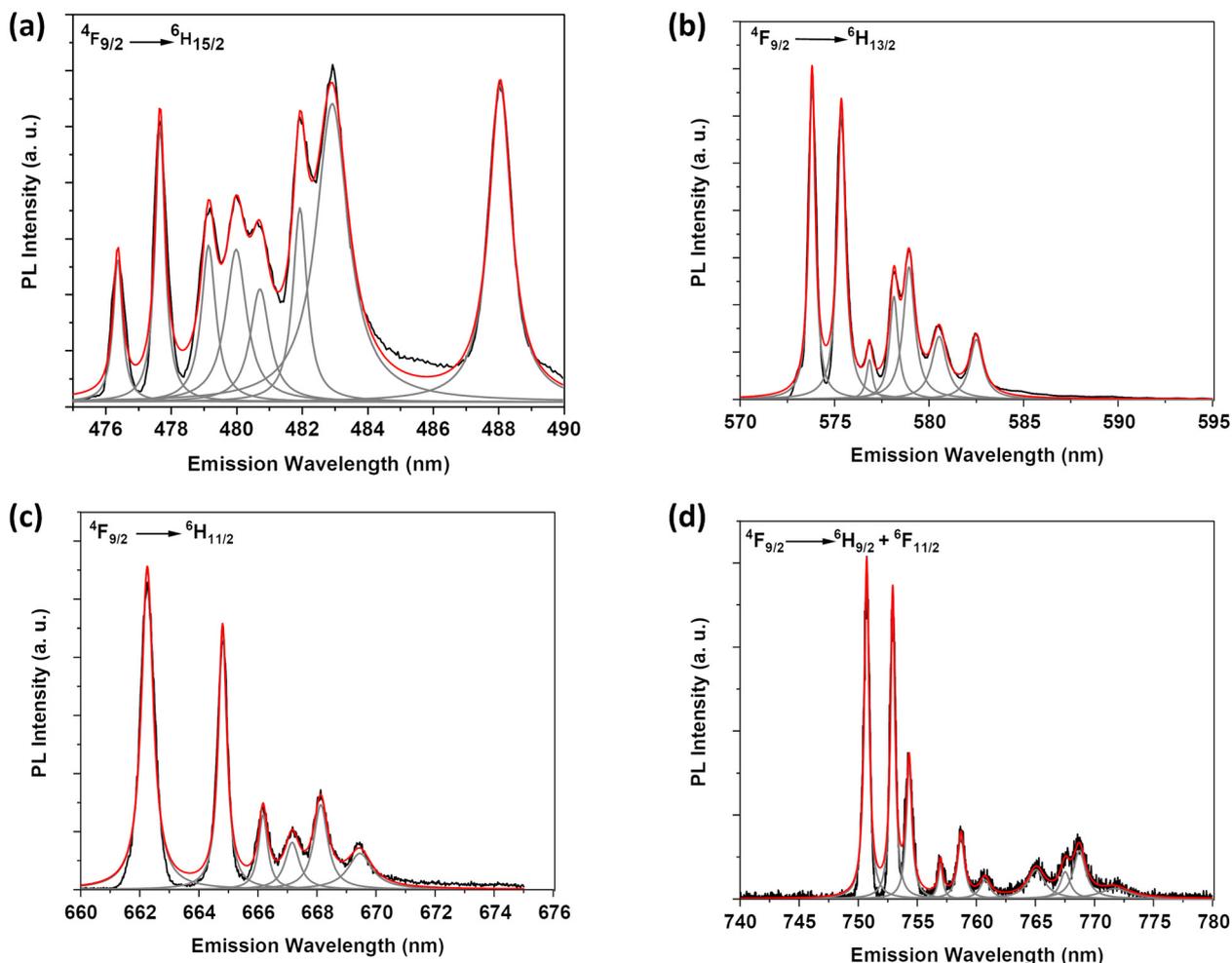

Fig. 8 Deconvoluted PL spectra of the stoichiometric Dy(III) compound (**1**) recorded at 2.4 K. (a) $^4F_{9/2} \rightarrow {}^6H_{15/2}$ transition, (b) $^4F_{9/2} \rightarrow {}^6H_{13/2}$ transition, (c) $^4F_{9/2} \rightarrow {}^6H_{11/2}$ transition, and (d) $^4F_{9/2} \rightarrow {}^6H_{9/2}$ and $^4F_{9/2} \rightarrow {}^6F_{11/2}$ transitions. The black, red, and grey lines represent experimental data, overall fit, and individual Lorentzian components, respectively.

Table 2 Energy difference between the crystal-field split KDs of the $^6H_{15/2}$ state estimated from the PL spectrum of compound **1** measured at 2.4 K. The relative energy represents the position of excited states relative to the ground state

KD	Peak position (nm cm^{--1})	Relative energy (cm^{-1})
1	476.4/20 990.8	0
2	477.7/20 933.6	57.2
3	479.2/20 868.1	122.7
4	480/20 833.3	157.5
5	480.7/20 803	187.8
6	481.9/20 751.2	239.6
7	482.9/20 708.2	282.6
8	488.1/20 487.6	503.2

Lorentz functions and tentatively attributed to the $^4F_{9/2} \rightarrow$ $^6H_{9/2}$ transition (Fig. 8d). The remaining ones are attributed to the $^4F_{9/2} \rightarrow$ $^6F_{11/2}$ transition based on a literature report.[87] The magnitude of crystal field splitting in the $^6H_{13/2}$, $^6H_{11/2}$, and $^6H_{9/2}$ states is 260.3 cm^{-1}, 162.4 cm^{-1}, and 140.5 cm^{-1}, respectively. As expected, the magnitude of crystal field splitting decreases with decreasing J values. The above analysis allowed us to estimate the energy separation between the m_J sublevels of the $^6H_{13/2}$ (Table S15), $^6H_{11/2}$ (Table S16), and $^6H_{9/2}$ (Table S17) states.

Computational studies

In order to unambiguously assign the transitions with true nature of m_J states and compare the experimental energy separation between the CF split KDs with calculated ones, computational studies have been performed and the PL spectrum of compound **1** has been simulated (see Fig. 9 and Fig. S50). The compound unit as shown in Fig. 2a is used as a model compound for the calculation. The system's states have been obtained using our inhouse developed complete active space spin orbit configuration Interaction (CASOCI) program[73] using an x2c-TZVP all-electron basis[88] for the Dy(III) centre and def2-TZVP basis[69] for the surrounding ligands. Technically, the calculation yields wavefunctions and energies of all electronic

states with nine electrons in the 4f shell of Dy. Between all these states, the transition energies and transition moments can be obtained in a similar way to that in the work of Zakrzewski *et al.*[89]

Due to the neglect of the dynamic correlation energy in the CASOCI calculations, the higher LS terms are not as well described as the ground state, particularly $^4F_{9/2}$ which is located at 20 990 cm^{-1} in experiment and at 24 306 cm^{-1} in the calculation. It cannot be expected that the relative energies and compositions of the five Kramers doublets are correctly described. Therefore, we averaged over the energies of all Kramers doublets of the $^4F_{9/2}$ state assuming a degeneracy and shifted them down to the experimental transition energy to the $^6H_{15/2}$ and calculated the transitions into the individual Kramers doublets of the different ^6H_J states.

To assign the observed optical transitions, oscillator strengths using the dipole-length formula (eqn (3))[90,91] have been implemented in the CASOCI-program for transitions between the calculated states.

$$f_{ij}^l = \frac{2}{3}\left(E_j - E_i\right)|\langle j|\hat{\mu}|i\rangle|^2 \tag{3}$$

Here, the oscillator strength f_{ij}^l between the states i and j in the length formalism is dependent on the energies of the initial and final states $E_{i,j}$ and the square of the transition dipole moment $\langle j|\hat{\mu}|i\rangle$. We can do this in a straightforward manner as the full diagonalization of the Hamilton operator gives us access to explicit expressions for each wavefunction and the respective integrals. As recently reported, the energies of excited states in CASOCI are overestimated due to missed charge transfer states and a lack of dynamic correlation.[92] Therefore, the excited states belonging to other ^6H_J terms of the free ion were shifted down to the experimental level obtained from the PL measurements, which is also very close to the values for the free ion reported by NIST.[93] Lastly, the obtained oscillator strengths are then scaled and convoluted with gaussians (σ = 10 cm^{-1}) to fit the experimental spectrum.
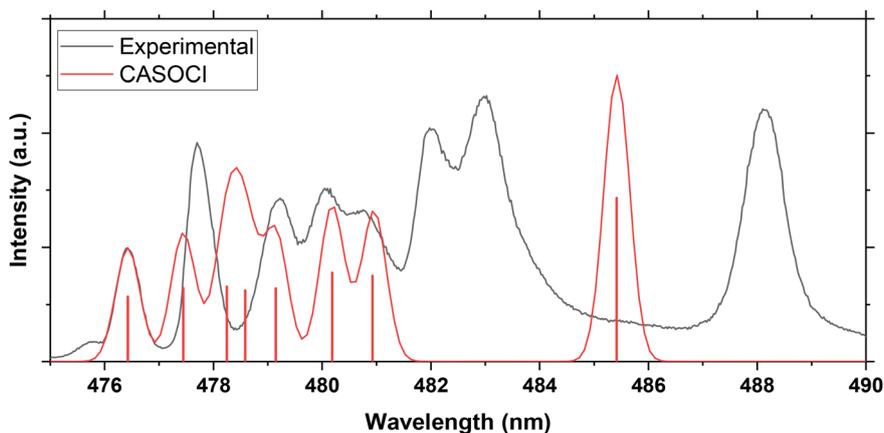

Fig. 9 Comparison of experimental (black) and computed (red) PL spectra corresponding to the $^4F_{9/2} \rightarrow$ $^6H_{15/2}$ ground state multiplet. Oscillator strengths are depicted as red bars.

Table 3 Experimental and calculated CF splitting energies and m_J composition of the $^6H_{15/2}$ multiplet of Dy(III) in compound **1**. The m_J contributions ≥5% for each KD are given

Exp. position (cm^{-1})	Exp./CASOCI energy (cm^{-1})	m_J composition
20 990.8	0.0/0.0	86.8%$\|\pm15/2\rangle$ + 6.9%$\|\pm11/2\rangle$
20 933.6	57.2/45.7	6.2%$\|\pm13/2\rangle$ + 5.0%$\|\pm9/2\rangle$ + 16.1%$\|\pm5/2\rangle$ + 26.9%$\|\pm3/2\rangle$ + 34.2%$\|\pm1/2\rangle$
20 868.1	122.7/79.9	49.6%$\|\pm13/2\rangle$ + 26.3%$\|\pm11/2\rangle$ + 9.0%$\|\pm7/2\rangle$ + 7.0%$\|\pm3/2\rangle$
20 833.3	157.5/95.1	14.1%$\|\pm13/2\rangle$ + 14.0%$\|\pm11/2\rangle$ + 36.4%$\|\pm9/2\rangle$ + 8.5%$\|\pm7/2\rangle$ + 17.0%$\|\pm5/2\rangle$ + 5.8%$\|\pm3/2\rangle$
20 803	187.8/119.4	13.9%$\|\pm11/2\rangle$ + 21.3%$\|\pm9/2\rangle$ + 38.2%$\|\pm7/2\rangle$ + 9.9%$\|\pm5/2\rangle$ + 7.6%$\|\pm1/2\rangle$
20 751.2	239.6/164.8	7.0%$\|\pm9/2\rangle$ + 23.0%$\|\pm7/2\rangle$ + 36.1%$\|\pm5/2\rangle$ + 23.4%$\|\pm3/2\rangle$ + 6.6%$\|\pm1/2\rangle$
20 708.2	282.6/197.9	5.0%$\|\pm7/2\rangle$ + 15.7%$\|\pm5/2\rangle$ + 32.5%$\|\pm3/2\rangle$ + 44.1%$\|\pm1/2\rangle$
20 487.6	503.2/388.1	6.3%$\|\pm15/2\rangle$ + 22.7%$\|\pm13/2\rangle$ + 31.8%$\|\pm11/2\rangle$ + 23.9%$\|\pm9/2\rangle$ + 11.1%$\|\pm7/2\rangle$

For further analysis, the contribution of pure m_J states to each KD was computed as summarized in Table 3 for the $^6H_{15/2}$ term and Table S17 for the remaining terms. In order to do so, we have used the ground state KD-main axis as the reference coordinate system for all higher lying states, diagonalizing the J_z-operator within each spin–orbit coupled multiplet individually, assuming that they cannot mix.

Overall, the comparison of the calculated data with the PL study showed that a good agreement can be reached at this level of calculation. Numerous factors have to be considered for the spectrum: it is generally known that methods on the CASSCF level underestimate the crystal field splitting.[94] We have not corrected for this underestimation since this would be more or less arbitrary. Consequently, the peak intensities need to be compared. The most dominant is the large intensity for the highest KD at 388 cm^{-1} (calculated). This peak (λ_{max} = ca. 488 nm) correlates well with the secluded feature in the PL study. Going to higher energies (lower wavelengths) a distinct double, followed by a triple and a subsequent single feature can be compared in peak size. The energy difference between the 3rd and 4th KD is underestimated in the calculation showing as one large peak.

In the following, we present a discussion on the parameters contributing to the magnetization relaxation in the Dy(III) compound. An important parameter governing the magnetization relaxation is the LF symmetry around the Dy(III) centre.[65,95] The C_{2v} LF symmetry around Dy(III) is expected to facilitate QTM, as observed for the stoichiometric compound under zero applied magnetic field (H_{DC} = 0). The distorted LF reflects as large transversal components of the diagonalized g-tensor (g_x = 0.134; g_y = 0.195; g_z = 18.874) in the ground state KD1. The CF parameters (B_q^k) collected in Table S18 show that the non-axial terms ($q \neq 0$ and k = 2, 4) are stronger than axial terms (q = 0 and k = 2, 4). These facets indicate that the distorted LF symmetry induces fast QTM leading to magnetization relaxation through the ground m_J = ±15/2 states in the stoichiometric form of compound **1**.

Large transverse components facilitate spin–flip transitions between neighbouring Dy(III) centres via dipolar interactions (J_{dip}).[75] We have calculated the dipolar coupling constants, employing computational methods, to the five nearest neighbours in the crystal lattice as depicted in Fig. 10. The nearest Dy-centres are at a distance between 9.7 Å and 10.5 Å from the central ion. However, such magnitudes are enough to lift the degeneracy of the lowest KDs giving an efficient pathway for QTM.

The relaxation times of QTM can be approximated using two formulas proposed by Yin et al.[96] and Prokof'ev and Stamp.[97–99] The formulas we used are given in the SI. Assuming the suggested average internal B-field of 20 mT, tunnelling times between 2.4 × 10^{-7} s and 1.2 × 10^{-6} s are obtained. These are too low compared to the experiment, but also consider that a significant internal B-field should be present as discussed above. However, it has been shown that the inclusion of an anisotropic internal B-field could remedy this discrepancy.[100]

Increasing the mean distance between Dy(III) centres would decrease the QTM efficiency as observed in the dynamic magnetic studies of the diluted **1@Y** compound. Although the absence of QTM is observed for the **1@Y** compound in the AC studies, it is limited by the instrumental limitations because the χ'' peaks are only observable from 2.8 K for the compound. This indicates that QTM could be present at temperatures lower than 2.8 K. The observation of a waist restricted hysteresis loop in the M versus H studies, performed at 1.8 K, clearly indicates the presence of QTM in the **1@Y** sample. In hindsight, we attribute the dominant QTM relaxation channel in the stoichiometric compound to the inherently low-site symmetry around Dy(III), causing large transversal components of g and weak intermolecular dipolar interactions. The dipolar interactions are mitigated by diluting the magnetically active Dy(III) centre in the Y(III) matrix. An applied DC field has further suppressed QTM, as discussed before.

From the AC studies of **1@Y** at H_{DC} = 0 Oe an effective barrier of 77.13 K (53.62 cm^{-1}) is obtained. The value matches well with the energy observed for the first excited KD in the PL study (57.2 cm^{-1}, Table 2). The energies compare well with the energy of the first excited KD obtained from CASOCI calculations (45.7 cm^{-1}, Table 3). The diagonalized g-tensor of the first excited KD (g_x = 0.753; g_y = 1.344; g_z = 16.730) obtained from the calculations indicates that the predominant relaxation pathway in the diluted sample (**1@Y**) is temperature-activated QTM (TA-QTM) via the first excited state. The contribution of each m_J component to the respective states obtained from CASOCI calculations provided further insights into the magnetization relaxation mechanism of compound **1**. There
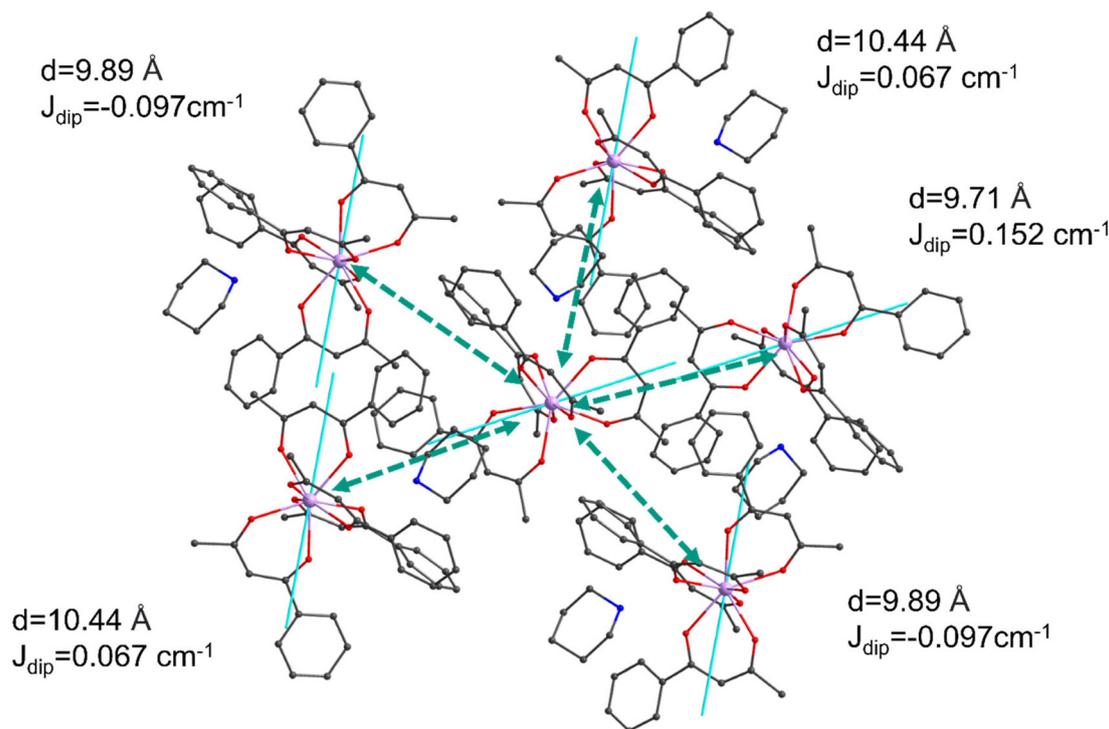
d=9.89 Å
J_{dip}=-0.097cm⁻¹

d=10.44 Å
J_{dip}=0.067 cm⁻¹

d=9.71 Å
J_{dip}=0.152 cm⁻¹

d=10.44 Å
J_{dip}=0.067 cm⁻¹

d=9.89 Å
J_{dip}=-0.097cm⁻¹

Fig. 10 Intermolecular dipolar interaction in the crystal lattice of **1**. The dipolar coupling between the ground state KDs is smaller than 0.15 cm^{-1} in all cases.

are significant contributions from m_J states to the ground state other than $m_J = \pm 15/2$. Besides the main contribution of 86.8% of $m_J = \pm 15/2$, the 11/2-state contributes with 6.9% to the ground state wavefunction. This small contribution is enough to induce QTM. In contrast, the first excited KD is a strong mixture of a number of m_J states, mainly 5/2 (16.1%), 3/2 (26.9%), and 1/2 (34.2%). This explains why this KD poses as an upper barrier for the relaxation dynamics. As soon as this state is populated by temperature, the magnetization relaxes *via* it.

β-Diketone coordinated Dy(III) compounds (see Fig. S51 for structures) offer a possibility to tune the magnetic and luminescence properties of the compounds by varying the nature of the β-diketone ligand and counter cation. On a comparative scale, the μ_{eff} value observed for the undiluted compound **1** at $H_{DC} = 1000$ Oe is one of the best among the values reported for tetrakis β-diketone coordinated Dy(III) compounds (Table 4). For the diluted compound—**1@Y**—$\mu_{eff} = 53.62$ cm^{-1} is observed, the value is the best so far reported for [Dy(L)₄](X) type compounds in the absence of an applied DC field.

For the [Dy(L)₄](X) compounds listed in Table 4, the LF symmetry of either D_{4d} or D_{2d} is obtained from the SHAPE analysis. However, the magnetization relaxation of the compounds vastly differs from each other due to the presence of differing nature of counter cations and β-diketone ligands. Notable examples are compounds [Dy(DBM)₄](Hex₄N) and [Dy(DBM)₄] (Et₄N) featuring distinct SMM characteristics despite having the same D_{4d} LF geometry around the Dy(III) center.

Table 4 Energy barriers (μ_{eff}) for magnetization relaxation associated with tetrakis-β-diketone compounds [Dy(L)₄](X)

S. no.	Molecular formula	SHAPE Geometry	U_{eff} (cm^{-1})	Ref.
1	[Dy(BA)₄](pip) (**1**)/(**1@Y**)	D_{4d}	70.75 ($H_{DC} = 1000$ Oe)/53.62 ($H_{DC} = 0$ Oe)	This study
2	[Dy(DBM)₄] (Hex₄N)	D_{4d}	19.25 ($H_{DC} = 0$ Oe)	63
3	[Dy(DBM)₄] (But₄N)	D_{4d} (Dy₁); D_{2d} (Dy₂)	40.1 ($H_{DC} = 0$ Oe); 81.32 ($H_{DC} = 2000$ Oe);	65
4	[Dy(DBM)₄] (Et₄N)	D_{4d}	6.74 ($H_{DC} = 2000$ Oe)	65
5	[Dy(DBM)₄] (PhCH₂N(CH₃)₃)	D_{4d}	15.71 ($H_{DC} = 900$ Oe)	65
6	[Dy(TTA)₄] (Hex₄N)	D_{4d}	29.61 ($H_{DC} = 700$ Oe)	65
7	[Dy(hfac)₄](Cs)	D_{2d}	Not an SMM	62
8	[Dy(hfac)₄](K)	D_{4d}	16.65 ($H_{DC} = 2000$ Oe)	62
9	[(L)Dy(tta)₄][Fe (tta)]	D_{nd}	Not reported	101
10	[Dy(btfa)₄](acr)	D_{2d}	40.5 ($H_{DC} = 1000$ Oe)	64

Remarkably, strong QTM is observed for the undiluted compounds at $H_{DC} = 0$, indicating the fact that the LF geometry in the compounds could be more distorted than the D_{4d}, allowing QTM. The above points emphasize the fact that small structural variations in the first coordination sphere around the Dy

(III) center and the consequent LF variation significantly affect the nature of the spin-relaxation process in [Dy(L)$_4$](X) compounds. In order to unambiguously elucidate the effective LF around the Dy(III) center, the emission spectrum of the isostructural Eu(III) compound can be analyzed, as demonstrated in this study. It would be interesting to study magnetization relaxation in a series of Dy(III) compounds featuring the same β-diketone ligand and different counter cations. Such a series has already been reported for Eu(III) compounds composed of the benzoylacetonate ligand and differing in the alkali metal counter cations, allowing one to establish effective LF symmetry around the Dy(III) centers.

Apart from the magneto-optical correlations, the observation of clear splitting between the ^6H_J (J = 15/2, 13/2, 11/2, or 9/2) levels is quite interesting and rarely observed, especially when a commercially available spectrometer with a continuous light source is used. As can be seen in Fig. 8, one can easily count the number of CF transitions associated with each level simply by visual inspection. We attribute such resolution to narrow-linewidths associated with the optical transitions. In our previous study dealing with the Eu(III) compound **2**, an ultra-narrow $^5D_0 \rightarrow {}^7F_0$ inhomogeneous linewidth of 6.6 GHz (0.007 nm) is estimated, attributed to high-crystalline quality. Compound **2** is a well-known laser chelate investigated in the 1960s. In one of the seminal reports, Brecher *et al.*[102] noted that the presence of a charge balancing piperidinium cation restricts the conformational fluctuations of the ligands around the Eu(III). Consequently, sharp emission lines are observed. The same argument can be extrapolated to compound **1** considering the isostructural nature of compounds **1** and **2** and such conformational restrictions could be assigned as one of the contributing factors causing sharp emissions in compound **1**. The sharp and well-separated CF transitions observed for the compound also allow the estimation of inhomogeneous linewidths associated with each CF transition. The fullwidth at half maximum (FWHM) obtained from the Lorentz deconvolution procedure serves the purpose and linewidths associated with each CF transition can be seen in Fig. S46–S49. However, the values need to be noted with caution because the experimental linewidth depends on the bandpass used during the measurements. Considering the used emission bandpass of 0.27 nm and 1200 lines per mm in the gratings, we estimate the upper resolution of the spectrometer as 0.3 nm. Such estimate indicates that 0.3 nm is the lowest possible width that could be estimated. This indeed is true considering the FWHMs in the range of 0.3 estimated for transitions collected in Fig. S46–S49. On the other hand, the FWHMs estimated above 1 nm are caused by intrinsic factors associated with parameters such as molecular structure and crystal quality. In the unlucky situation of weak emission intensities, a wider bandpass is required to obtain reasonable intensity, leading to instrumental broadening of the linewidths masking the intrinsic broadening. One important consequence of this discussion is that the real linewidth of a transition that lies below the instrument limited linewidth could only be estimated from high-resolution laser spectroscopic

studies. These points also emphasize the need for reporting the bandpass and parameters such as step size used to collect PL data, a smaller step size relative to bandpass improves the resolution.

The spin-bearing nature of Dy(III)'s $^6H_{15/2}$ ground state also plays a role in modulating the observed linewidths of optical transitions. With a large total angular momentum (J = 15/2), Dy(III) possesses sublevels that are highly sensitive to local crystal field perturbations. This sensitivity enhances the resolution of crystal field–split transitions, but also renders them susceptible to inhomogeneous broadening arising from site-to-site variations. Moreover, the substantial magnetic moment of Dy(III) introduces dipole–dipole interactions with neighbouring paramagnetic centres (as discussed before) and magnetic nuclei, contributing to static field fluctuations that broaden emission lines. Hyperfine coupling with isotopes such as ^{161}Dy (I = 5/2) may further complicate the spectral analysis, although such effects are typically unresolved in conventional photoluminescence measurements due to the large inhomogeneous broadening of the emission lines. Compared to Eu(III) compounds, which exhibit ultra-narrow transitions due to their J = 0 ground state, Dy(III) compounds inherently show broader linewidths unless the crystallinity and site symmetry are exceptionally well-controlled. These considerations underscore the importance of disentangling intrinsic and instrumental contributions to linewidths, particularly when interpreting CF transitions in spin-bearing lanthanide systems.

Conclusions

We provide a detailed correlation between structure, single-molecule magnetism and photoluminescence for the mononuclear Dy(III) compound **1**. The stoichiometric compound **1** is a zero-field SMM and quantum tunnelling of magnetization (QTM) is the dominant relaxation process in the absence of an applied DC magnetic field. As expected, application of an external DC field mitigated the QTM and the spin-reversal in **1** proceeded following Orbach and Raman mechanisms. Dilution of compound **1** in the isostructural Y(III) lattice mitigated QTM and at zero applied field (H_{DC} = 0), Raman and Orbach processes spur the magnetization reversal. A comparison between the U_{eff} values estimated from the AC studies at H_{DC} = 0 and the LF splitting energies estimated from PL studies indicates that magnetization relaxation in the diluted sample proceeds through the first excited sub-level of the $^6H_{15/2}$ ground state manifold, validated by CASOCI calculations.

Remarkably, the well-resolved nature of the CF splitting associated with compound **1** allowed us to use it as a benchmark to validate the appropriateness of the computational methodologies in determining the LF splitting and luminescence spectrum. Though dynamic correlation is not included in the calculations, the splitting of the different terms of ^6H_J into sub-levels is reasonably well described. Crucially, the

absence of Dy(III) emission at RT and its emergence at cryogenic temperatures indicate the possibility that compounds that are non-emissive at RT could be emissive at cryogenic temperatures, one doesn't need to be disheartened seeing no emission at RT. The isostructural relationship between the Dy(III) and Eu(III) analogous facilitates the assignment of effective LF symmetry around the Dy(III) offering a methodology to elucidate accurate magneto-structural correlations. However, the requirement of an isostructural Eu(III) and Dy(III) pair is a constrain, as lanthanide contraction may preclude the formation of isostructural pairs.

The utility of $[Ln(L)_4](X)$ (Ln = Eu(III) and Er(III)) compounds as optically addressable platforms suitable for quantum information processing (QIP) applications has been demonstrated.[8,103,104] The presence of rich magnetic and optical properties as well as the structure tunablility of $[Ln(L)_4]$(X) type compounds indicate that systematic studies of this family of compounds are likely to yield novel materials platforms with compelling physical properties such as narrow optical linewidths and long optical and spin coherence times, useful for developing optically-addressable QIP platforms.[8,9,103]

Author contributions

S. K. K.: conceptualization, formal analysis, synthesis and characterization, magnetic and photoluminescence measurements, writing—original draft, reviewing and editing. C. P. and K. F.: computational studies, formal analysis, writing—original draft, reviewing and editing. Z. J.: preliminary magnetic measurements and computational studies, writing—original draft, reviewing and editing. S. P.: μ-SQUID studies. B. H.: high-resolution PXRD studies. O. F.: single-crystal X-ray diffraction studies. S. K.: SEM studies. W. W., A. K. P., K. F. and M. R.: supervision and funding acquisition.

Conflicts of interest

The authors declare no conflict of interest.

Data availability

All the data are available in the main script and the supplementary information (SI). Supplementary information: additional experimental details, synthesis and characterisation of ligands and compounds, and crystallographic data of compounds. See DOI: https://doi.org/10.1039/d6dt00081a.

Original datasets of magnetic and PL measurements can be found in this link: https://doi.org/10.5281/zenodo.17981253.

CCDC 2010809 (**1**) and 2441051 (**3**) contain the supplementary crystallographic data for this paper.[105a,b]

Acknowledgements

References

1 K. Bernot, Get under the Umbrella: A Comprehensive Gateway for Researchers on Lanthanide–Based Single–Molecule Magnets, *Eur. J. Inorg. Chem.*, 2023, **26**, e202300336.

2 J. D. Rinehart and J. R. Long, Exploiting single-ion anisotropy in the design of f-element single-molecule magnets, *Chem. Sci.*, 2011, **2**, 2078.

3 S. T. Liddle and J. Van Slageren, Improving f-element single molecule magnets, *Chem. Soc. Rev.*, 2015, **44**, 6655–6669.

4 D. N. Woodruff, R. E. P. Winpenny and R. A. Layfield, Lanthanide Single-Molecule Magnets, *Chem. Rev.*, 2013, **113**, 5110–5148.

5 J. Wang, C. Sun, Q. Zheng, D. Wang, Y. Chen, J. Ju, T. Sun, Y. Cui, Y. Ding and Y. Tang, Lanthanide Single–molecule Magnets: Synthetic Strategy, Structures, Properties and Recent Advances, *Chem. – Asian J.*, 2023, **18**, e202201297.

6 L. Sorace, C. Benelli and D. Gatteschi, Lanthanides in molecular magnetism: old tools in a new field, *Chem. Soc. Rev.*, 2011, **40**, 3092.

7 R. Marin, G. Brunet and M. Murugesu, Shining New Light on Multifunctional Lanthanide Single–Molecule Magnets, *Angew. Chem., Int. Ed.*, 2021, **60**, 1728–1746.

8 D. Serrano, S. K. Kuppusamy, B. Heinrich, O. Fuhr, D. Hunger, M. Ruben and P. Goldner, Ultra-narrow optical linewidths in rare-earth molecular crystals, *Nature*, 2022, **603**, 241–246.

9 S. K. Kuppusamy, D. Hunger, M. Ruben, P. Goldner and D. Serrano, Spin-bearing molecules as optically addressable platforms for quantum technologies, *Nanophotonics*, 2024, **13**, 4357–4379.

10 P. Fang, P. Huo, L. Wang, Z. Zhao, G. Yu, Y. Huang, Z. Bian and Z. Liu, Lanthanide complexes with d-f transition: new emitters for single-emitting-layer white

organic light-emitting diodes, *Light: Sci. Appl.*, 2023, **12**, 170.

11 A. J. Shin, C. Zhao, Y. Shen, C. E. Dickerson, B. Li, H. Roshandel, D. Bím, T. L. Atallah, P. H. Oyala, Y. He, L. K. Alson, T. A. Kerr, A. N. Alexandrova, P. L. Diaconescu, W. C. Campbell and J. R. Caram, Toward liquid cell quantum sensing: Ytterbium complexes with ultranarrow absorption, *Science*, 2024, **385**, 651–656.

12 R. Sessoli, D. Gatteschi, A. Caneschi and M. A. Novak, Magnetic bistability in a metal-ion cluster, *Nature*, 1993, **365**, 141–143.

13 G. Christou, D. Gatteschi, D. N. Hendrickson and R. Sessoli, Single-Molecule Magnets, *MRS Bull.*, 2000, **25**, 66–71.

14 N. Ishikawa, M. Sugita, T. Ishikawa, S. Koshihara and Y. Kaizu, Lanthanide Double-Decker Complexes Functioning as Magnets at the Single-Molecular Level, *J. Am. Chem. Soc.*, 2003, **125**, 8694–8695.

15 N. F. Chilton, Molecular Magnetism, *Annu. Rev. Mater. Res.*, 2022, **52**, 79–101.

16 N. F. Chilton, *Ab initio* electronic structure calculations of lanthanide single-molecule magnets; a practical guide, *Chem. Soc. Rev.*, 2025, **54**, 11468–11487.

17 V. Sirenko, F. Bartolomé Usieto and J. Bartolomé, The paradigm of magnetic molecule in quantum matter: Slow molecular spin relaxation, *Low Temp. Phys.*, 2024, **50**, 431–445.

18 D. Stepanenko, M. Trif and D. Loss, Quantum computing with molecular magnets, *Inorg. Chim. Acta*, 2008, **361**, 3740–3745.

19 M. N. Leuenberger and D. Loss, Quantum computing in molecular magnets, *Nature*, 2001, **410**, 789–793.

20 E. Moreno-Pineda and W. Wernsdorfer, Measuring molecular magnets for quantum technologies, *Nat. Rev. Phys.*, 2021, **3**, 645–659.

21 E. Moreno-Pineda, C. Godfrin, F. Balestro, W. Wernsdorfer and M. Ruben, Molecular spin qudits for quantum algorithms, *Chem. Soc. Rev.*, 2018, **47**, 501–513.

22 W. Wernsdorfer and M. Ruben, Synthetic Hilbert Space Engineering of Molecular Qu *d* its: Isotopologue Chemistry, *Adv. Mater.*, 2019, **31**, 1806687.

23 A. K. Boudalis, The Ever-Higher Blocking Temperature: Misconceptions and Self-Defeating Successes in Single-Molecule Magnetism, *Inorg. Chem.*, 2025, **64**(50), 24345–24350.

24 S. K. Gupta, T. Rajeshkumar, G. Rajaraman and R. Murugavel, An air-stable Dy(iii) single-ion magnet with high anisotropy barrier and blocking temperature, *Chem. Sci.*, 2016, **7**, 5181–5191.

25 F. Guo, B. M. Day, Y. Chen, M. Tong, A. Mansikkamäki and R. A. Layfield, A Dysprosium Metallocene Single–Molecule Magnet Functioning at the Axial Limit, *Angew. Chem., Int. Ed.*, 2017, **56**, 11445–11449.

26 F.-S. Guo, B. M. Day, Y.-C. Chen, M.-L. Tong, A. Mansikkamäki and R. A. Layfield, Magnetic hysteresis up to 80 kelvin in a dysprosium metallocene single-molecule magnet, *Science*, 2018, **362**, 1400–1403.

27 V. Vieru, S. Gómez-Coca, E. Ruiz and L. F. Chibotaru, Increasing the Magnetic Blocking Temperature of Single–Molecule Magnets, *Angew. Chem., Int. Ed.*, 2024, **63**, e202303146.

28 C. A. P. Goodwin, F. Ortu, D. Reta, N. F. Chilton and D. P. Mills, Molecular magnetic hysteresis at 60 kelvin in dysprosocenium, *Nature*, 2017, **548**, 439–442.

29 J. P. Durrant, B. M. Day, J. Tang, A. Mansikkamäki and R. A. Layfield, Dominance of Cyclobutadienyl Over Cyclopentadienyl in the Crystal Field Splitting in Dysprosium Single–Molecule Magnets, *Angew. Chem.*, 2022, **134**, e202200525.

30 C. A. Gould, K. R. McClain, D. Reta, J. G. C. Kragskow, D. A. Marchiori, E. Lachman, E.-S. Choi, J. G. Analytis, R. D. Britt, N. F. Chilton, B. G. Harvey and J. R. Long, Ultrahard magnetism from mixed-valence dilanthanide complexes with metal-metal bonding, *Science*, 2022, **375**, 198–202.

31 K. Randall McClain, C. A. Gould, K. Chakarawet, S. J. Teat, T. J. Groshens, J. R. Long and B. G. Harvey, High-temperature magnetic blocking and magneto-structural correlations in a series of dysprosium(iii) metallocenium single-molecule magnets, *Chem. Sci.*, 2018, **9**, 8492–8503.

32 P. Evans, D. Reta, G. F. S. Whitehead, N. F. Chilton and D. P. Mills, Bis-Monophospholyl Dysprosium Cation Showing Magnetic Hysteresis at 48 K, *J. Am. Chem. Soc.*, 2019, **141**, 19935–19940.

33 J. Emerson-King, G. K. Gransbury, B. E. Atkinson, W. J. A. Blackmore, G. F. S. Whitehead, N. F. Chilton and D. P. Mills, Soft magnetic hysteresis in a dysprosium amide–alkene complex up to 100 kelvin, *Nature*, 2025, **643**, 125–129.

34 J. Emerson-King, J. Baldwin, S. C. Corner, W. J. A. Blackmore, N. F. Chilton and D. P. Mills, Magnetic Hysteresis up to 73 K in a Dysprosium Cyclopentadienyl-Amide Single-Molecule Magnet, *J. Am. Chem. Soc.*, 2025, **147**, 35555–35566.

35 R. L. Ahlefeldt, N. B. Manson and M. J. Sellars, Optical lifetime and linewidth studies of the transition in: A potential material for quantum memory applications, *J. Lumin.*, 2013, **133**, 152–156.

36 F. Chiossi, D. Serrano, A. Tiranov and P. Goldner, High-resolution optical spectroscopy of europium nitrate hexahydrate crystals, *J. Lumin.*, 2025, **288**, 121500.

37 J.-C. G. Bünzli and K.-L. Wong, Lanthanide photonics on the path to future: from gas lighting to optical computers, *J. Lumin.*, 2025, **287**, 121473.

38 S. V. Eliseeva, A reflection on "Intriguing aspects of lanthanide luminescence", *Chem. Sci.*, 2026, **17**, 20–26.

39 G. Cucinotta, M. Perfetti, J. Luzon, M. Etienne, P. Car, A. Caneschi, G. Calvez, K. Bernot and R. Sessoli, Magnetic Anisotropy in a Dysprosium/DOTA Single–Molecule Magnet: Beyond Simple Magneto–Structural Correlations, *Angew. Chem., Int. Ed.*, 2012, **51**, 1606–1610.

40 M. Boulon, G. Cucinotta, J. Luzon, C. Degl'Innocenti, M. Perfetti, K. Bernot, G. Calvez, A. Caneschi and R. Sessoli, Magnetic Anisotropy and Spin–Parity Effect Along the Series of Lanthanide Complexes with DOTA, *Angew. Chem., Int. Ed.*, 2013, **52**, 350–354.

41 N. Jain, G. David, M. Cordier, Y. Suffren, B. L. Guennic, Y. Sarazin and K. Bernot, Magneto–Optical Correlations in a High Symmetry Dysprosium Complex Reveal an Almost "Ideal Non–SMM" and Orange–to–Red DyIII –Based Emitter, *ChemistryEurope*, 2025, **3**, e202500193.

42 F. Pointillart, B. L. Guennic, S. Golhen, O. Cador, O. Maury and L. Ouahab, A redox-active luminescent ytterbium based single molecule magnet, *Chem. Commun.*, 2013, **49**, 615–617.

43 G. Brunet, R. Marin, M.-J. Monk, U. Resch-Genger, D. A. Gálico, F. A. Sigoli, E. A. Suturina, E. Hemmer and M. Murugesu, Exploring the dual functionality of an ytterbium complex for luminescence thermometry and slow magnetic relaxation, *Chem. Sci.*, 2019, **10**, 6799–6808.

44 J. Wang, J. J. Zakrzewski, M. Zychowicz, Y. Xin, H. Tokoro, S. Chorazy and S. Ohkoshi, Desolvation–Induced Highly Symmetrical Terbium(III) Single–Molecule Magnet Exhibiting Luminescent Self–Monitoring of Temperature, *Angew. Chem., Int. Ed.*, 2023, **62**, e202306372.

45 C. Harriswangler, F. Lucio-Martínez, L. Godec, L. K. Soro, S. Fernández-Fariña, L. Valencia, A. Rodríguez-Rodríguez, D. Esteban-Gómez, L. J. Charbonnière and C. Platas-Iglesias, Effect of Magnetic Anisotropy on the¹ H NMR Paramagnetic Shifts and Relaxation Rates of Small Dysprosium(III) Complexes, *Inorg. Chem.*, 2023, **62**, 14326–14338.

46 N. Kofod, R. Arppe-Tabbara and T. J. Sørensen, Electronic Energy Levels of Dysprosium(III) ions in Solution. Assigning the Emitting State and the Intraconfigurational 4f–4f Transitions in the Vis–NIR Region and Photophysical Characterization of Dy(III) in Water, Methanol, and Dimethyl Sulfoxide, *J. Phys. Chem. A*, 2019, **123**, 2734–2744.

47 C. E. Jackson, I. P. Moseley, R. Martinez, S. Sung and J. M. Zadrozny, A reaction-coordinate perspective of magnetic relaxation, *Chem. Soc. Rev.*, 2021, **50**, 6684–6699.

48 L. Gu and R. Wu, Origin of the anomalously low Raman exponents in single molecule magnets, *Phys. Rev. B*, 2021, **103**, 014401.

49 L. Gu and R. Wu, Origins of Slow Magnetic Relaxation in Single-Molecule Magnets, *Phys. Rev. Lett.*, 2020, **125**, 117203.

50 S. Alvarez, P. Alemany, D. Casanova, J. Cirera, M. Llunell and D. Avnir, Shape maps and polyhedral interconversion paths in transition metal chemistry, *Coord. Chem. Rev.*, 2005, **249**, 1693–1708.

51 V. R. M. Nielsen and T. Just Sørensen, Determining molecular structure, coordination geometry, and molecular symmetry using a continuous symmetry operation measure software, *Nat. Commun.*, DOI: 10.1038/s41467-025-66054-7.

52 K. Binnemans, Interpretation of europium(III) spectra, *Coord. Chem. Rev.*, 2015, **295**, 1–45.

53 P. A. Tanner, Some misconceptions concerning the electronic spectra of tri-positive europium and cerium, *Chem. Soc. Rev.*, 2013, **42**, 5090.

54 P. Serna-Gallén, H. Beltrán-Mir and E. Cordoncillo, Practical guidance for easily interpreting the emission and physicochemical parameters of Eu3+ in solid-state hosts, *Ceram. Int.*, 2023, **49**, 41078–41089.

55 J.-C. G. Bünzli and G.-O. Pradervand, The Eu(III) ion as luminescent probe: Laser-spectroscopic investigation of the metal ion sites in an 18-crown-6 complex, *J. Chem. Phys.*, 1986, **85**, 2489–2497.

56 C. D. E. S. Barbosa, L. L. Da Luz, F. A. A. Paz, O. L. Malta, M. O. Rodrigues, S. A. Júnior, R. A. S. Ferreira and L. D. Carlos, Site-selective Eu(iii) spectroscopy of highly efficient luminescent mixed-metal Pb(ii)/Eu(iii) coordination polymers, *RSC Adv.*, 2017, **7**, 6093–6101.

57 M. S. Thomsen, P. R. Nawrocki, N. Kofod and T. J. Sørensen, Seven Europium(III) Complexes in Solution – The Importance of Reporting Data When Investigating Luminescence Spectra and Electronic Structure, *Eur. J. Inorg. Chem.*, 2022, e202200334.

58 D. Marinotto, C. A. Marin, I. Rau, A. Colombo, F. Fagnani, D. Roberto and C. Dragonetti, Large Enhancement of the Luminescence Properties of an Eu(III) Dye upon Association with the DNA-CTMA Matrix, *Molecules*, 2025, **30**, 1395.

59 A. G. Bispo Jr., Multifunctional lanthanide(III) single-molecule magnets displaying luminescence thermometry: Progress, challenges, and future directions, *Coord. Chem. Rev.*, 2025, **537**, 216685.

60 L. R. Melby, N. J. Rose, E. Abramson and J. C. Caris, Synthesis and Fluorescence of Some Trivalent Lanthanide Complexes, *J. Am. Chem. Soc.*, 1964, **86**, 5117–5125.

61 Y. Duan, L. E. Rosaleny, J. T. Coutinho, S. Giménez-Santamarina, A. Scheie, J. J. Baldoví, S. Cardona-Serra and A. Gaita-Ariño, Data-driven design of molecular nanomagnets, *Nat. Commun.*, 2022, **13**, 7626.

62 D. Zeng, M. Ren, S.-S. Bao and L.-M. Zheng, Tuning the Coordination Geometries and Magnetic Dynamics of [Ln (hfac)₄]⁻ through Alkali Metal Counterions, *Inorg. Chem.*, 2014, **53**, 795–801.

63 W.-B. Sun, B. Yan, Y.-Q. Zhang, B.-W. Wang, Z.-M. Wang, J.-H. Jia and S. Gao, The slow magnetic relaxation regulated by ligand conformation of a lanthanide single-ion magnet [Hex₄ N][Dy(DBM)₄], *Inorg. Chem. Front.*, 2014, **1**, 503–509.

64 S. Speed, À. Tubau, R. Vicente, E. Castro and M. Font-Bardia, Slow Magnetic Relaxation and Luminescence Properties in Tetra β-Diketonate Lanthanide(III) Complexes, *Magnetochemistry*, 2023, **9**, 131.

65 Zhuo-Wu, Y.-M. Tian, P. Chen, W.-B. Sun, B.-W. Wang and S. Gao, A series of counter cation-dependent tetra β-diketonate mononuclear lanthanide(iii) single-molecule magnets and immobilization on pre-functionalised GaN

substrates by anion exchange reaction, *J. Mater. Chem. C*, 2021, **9**, 6911–6922.

66 T. G. Prokhorova, D. V. Korchagin, G. V. Shilov, A. I. Dmitriev, M. V. Zhidkov and E. B. Yagubskii, The Organic Ammonium Counterion Effect on Slow Magnetic Relaxation of the [Er(hfac)4]− Complexes, *Magnetochemistry*, 2023, **9**, 159.

67 W. Wernsdorfer, S. Bhaduri, R. Tiron, D. N. Hendrickson and G. Christou, Spin-Spin Cross Relaxation in Single-Molecule Magnets, *Phys. Rev. Lett.*, 2002, **89**, 197201.

68 A. D. Becke, A new mixing of Hartree–Fock and local density-functional theories, *J. Chem. Phys.*, 1993, **98**, 1372–1377.

69 F. Weigend and R. Ahlrichs, Balanced basis sets of split valence, triple zeta valence and quadruple zeta valence quality for H to Rn: Design and assessment of accuracy, *Phys. Chem. Chem. Phys.*, 2005, **7**, 3297.

70 S. G. Balasubramani, G. P. Chen, S. Coriani, M. Diedenhofen, M. S. Frank, Y. J. Franzke, F. Furche, R. Grotjahn, M. E. Harding, C. Hättig, A. Hellweg, B. Helmich-Paris, C. Holzer, U. Huniar, M. Kaupp, A. Marefat Khah, S. Karbalaei Khani, T. Müller, F. Mack, B. D. Nguyen, S. M. Parker, E. Perlt, D. Rappoport, K. Reiter, S. Roy, M. Rückert, G. Schmitz, M. Sierka, E. Tapavicza, D. P. Tew, C. van Wüllen, V. K. Voora, F. Weigend, A. Wodyński and J. M. Yu, TURBOMOLE: Modular program suite for *ab initio* quantum-chemical and condensed-matter simulations, *J. Chem. Phys.*, 2020, **152**, 184107.

71 C. van Wüllen, Relation between different variants of the generalized Douglas–Kroll transformation through sixth order, *J. Chem. Phys.*, 2004, **120**, 7307–7313.

72 C. van Wüllen and C. Michauk, Accurate and efficient treatment of two-electron contributions in quasirelativistic high-order Douglas-Kroll density-functional calculations, *J. Chem. Phys.*, 2005, **123**, 204113.

73 T. Bodenstein, A. Heimermann, K. Fink and C. van Wüllen, Development and Application of a Complete Active Space Spin–Orbit Configuration Interaction Program Designed for Single Molecule Magnets, *ChemPhysChem*, 2022, **23**, e202100648.

74 D. Casanova, M. Llunell, P. Alemany and S. Alvarez, The Rich Stereochemistry of Eight–Vertex Polyhedra: A Continuous Shape Measures Study, *Chem. – Eur. J.*, 2005, **11**, 1479–1494.

75 D. Aravena, Ab Initio Prediction of Tunneling Relaxation Times and Effective Demagnetization Barriers in Kramers Lanthanide Single-Molecule Magnets, *J. Phys. Chem. Lett.*, 2018, **9**, 5327–5333.

76 O. T. Alexander, R. E. Kroon, A. Brink and H. G. Visser, Symmetry correlations between crystallographic and photoluminescence study of ternary β-diketone europium (iii) based complexes using 1,10-phenanthroline as the ancillary ligand, *Dalton Trans.*, 2019, **48**, 16074–16082.

77 J. Blanc and D. L. Ross, Polarized Absorption and Emission in an Octacoordinate Chelate of Eu3+, *J. Chem. Phys.*, 1965, **43**, 1286–1289.

78 E. V. Sayre and S. Freed, Spectra and Quantum States of the Europic Ion in Crystals. I. Absorption Spectrum of Anhydrous Europic Chloride, *J. Chem. Phys.*, 1956, **24**, 1211–1212.

79 G. Jia, C. Wang and S. Xu, Local Site Symmetry Determination of Scheelite-Type Structures by Eu³⁺ Spectroscopy, *J. Phys. Chem. C*, 2010, **114**, 17905–17913.

80 W. Thor, A. N. Carneiro Neto, R. T. Moura, K.-L. Wong and P. A. Tanner, Europium(III) coordination chemistry: structure, spectra and hypersensitivity, *Coord. Chem. Rev.*, 2024, **517**, 215927.

81 D. Tu, Y. Liu, H. Zhu, R. Li, L. Liu and X. Chen, Breakdown of Crystallographic Site Symmetry in Lanthanide–Doped NaYF₄ Crystals, *Angew. Chem., Int. Ed.*, 2013, **52**, 1128–1133.

82 V. R. M. Nielsen, B. Le Guennic and T. J. Sørensen, , Evaluation of Point Group Symmetry in Lanthanide(III) Complexes: A New Implementation of a Continuous Symmetry Operation Measure with Autonomous Assignment of the Principal Axis, *J. Phys. Chem. A*, 2024, **128**, 5740–5751.

83 P. Li, Y. Guo, A. Liu, X. Yue, T. Yuan, J. Zhu, Y. Zhang and F. Li, Deterministic Relation between Optical Polarization and Lattice Symmetry Revealed in Ion-Doped Single Microcrystals, *ACS Nano*, 2022, **16**, 9535–9545.

84 L. J. Nugent, M. L. Bhaumik, S. George and S. M. Lee, Ligand Field Spectra of Some New Laser Chelates, *J. Chem. Phys.*, 1964, **41**, 1305–1312.

85 A. De Bettencourt-Dias, in *Luminescence of Lanthanide Ions in Coordination Compounds and Nanomaterials*, ed. A. De Bettencourt-Dias, Wiley, 1st edn, 2014, pp. 1–48.

86 J. J. Woods, A. Peterson, J. A. Adewuyi, R. Lai, J. N. Wacker, R. J. Abergel and G. Ung, Room temperature crystal field splitting of curium resolved by circularly polarized luminescence spectroscopy, *Chem. Sci.*, 2025, **16**, 4815–4820.

87 R. Shrivastava and S. Khaparde, Luminescence studies of diopside doped with various concentrations of Dysprosium(III), *Res. Chem. Intermed.*, 2022, **48**, 969–982.

88 P. Pollak and F. Weigend, Segmented Contracted Error-Consistent Basis Sets of Double- and Triple-ζ Valence Quality for One- and Two-Component Relativistic All-Electron Calculations, *J. Chem. Theory Comput.*, 2017, **13**, 3696–3705.

89 J. J. Zakrzewski, K. Kumar, M. Zychowicz, R. Jankowski, M. Wyczesany, B. Sieklucka, S. Ohkoshi and S. Chorazy, Combined Experimental and Ab Initio Methods for Rationalization of Magneto-Luminescent Properties of YbIII Nanomagnets Embedded in Cyanido/Thiocyanidometallate-Based Crystals, *J. Phys. Chem. Lett.*, 2021, **12**, 10558–10566.

90 S. Chandrasekhar, On the Continuous Absorption Coefficient of the Negative Hydrogen Ion, *Astrophys. J.*, 1945, **102**, 223.

91 M. T. Anderson and F. Weinhold, Relative accuracy of length and velocity forms in oscillator-strength calculations, *Phys. Rev. A*, 1974, **10**, 1457–1463.

92 M. Dahlen, N. Reinfandt, C. Jin, M. T. Gamer, K. Fink and P. W. Roesky, Hetero–bimetallic Lanthanide–Coinage Metal Compounds Featuring Possible Metal–Metal Interactions in the Excited State, *Chem. – Eur. J.*, 2021, **27**, 15128–15136.

93 W. C. Martin, R. Zalubas and L. Hagan, *Atomic energy levels - the rare-earth elements: the spectra of lanthanum, cerium, praseodymium, neodymium, promethium, samarium, europium, gadolinium, terbium, dysprosium, holmium, erbium, thulium, ytterbium, and lutetitum*, National Bureau of Standards, Gaithersburg, MD, 0 edn, 1978.

94 L. Ungur and L. F. Chibotaru, Ab Initio Crystal Field for Lanthanides, *Chem. – Eur. J.*, 2017, **23**, 3708–3718.

95 J.-L. Liu, Y.-C. Chen and M.-L. Tong, Symmetry strategies for high performance lanthanide-based single-molecule magnets, *Chem. Soc. Rev.*, 2018, **47**, 2431–2453.

96 B. Yin and C.-C. Li, A method to predict both the relaxation time of quantum tunneling of magnetization and the effective barrier of magnetic reversal for a Kramers single-ion magnet, *Phys. Chem. Chem. Phys.*, 2020, **22**, 9923–9933.

97 N. V. Prokof'ev and P. C. E. Stamp, Quantum relaxation of magnetisation in magnetic particles, *J. Low Temp. Phys.*, 1996, **104**, 143–209.

98 N. V. Prokof'ev and P. C. E. Stamp, Theory of the spin bath, *Rep. Prog. Phys.*, 2000, **63**, 669–726.

99 F. Luis, M. J. Martínez-Pérez, O. Montero, E. Coronado, S. Cardona-Serra, C. Martí-Gastaldo, J. M. Clemente-Juan, J. Sesé, D. Drung and T. Schurig, Spin-lattice relaxation via quantum tunneling in an Er 3 + -polyoxometalate molecular magnet, *Phys. Rev. B:Condens. Matter Mater. Phys.*, 2010, **82**, 060403.

100 B. Yin and L. Luo, The anisotropy of the internal magnetic field on the central ion is capable of imposing great impact on the quantum tunneling of magnetization of Kramers single-ion magnets, *Phys. Chem. Chem. Phys.*, 2021, **23**, 3093–3105.

101 S. Speed, F. Pointillart, J. Mulatier, L. Guy, S. Golhen, O. Cador, B. Le Guennic, F. Riobé, O. Maury and L. Ouahab, Photophysical and Magnetic Properties in Complexes Containing 3d/4f Elements and Chiral Phenanthroline–Based Helicate–Like Ligands, *Eur. J. Inorg. Chem.*, 2017, 2100–2111.

102 C. Brecher, H. Samelson and A. Lempicki, Laser Phenomena in Europium Chelates. III. Spectroscopic Effects of Chemical Composition and Molecular Structure, *J. Chem. Phys.*, 1965, **42**, 1081–1096.

103 E. Vasilenko, V. U. Chorakkunnath, J. Resch, N. Jobbitt, D. Serrano, P. Goldner, S. K. Kuppusamy, M. Ruben and D. Hunger, Optically detected nuclear magnetic resonance of coherent spins in a molecular complex, *arXiv*, 2025, preprint, arXiv:2509.01467, DOI: 10.48550/arXiv.2509.01467.

104 L. R. Weiss, G. T. Smith, R. A. Murphy, B. Golesorkhi, J. A. Méndez Méndez, P. Patel, J. Niklas, O. G. Poluektov, J. R. Long and D. D. Awschalom, A high-resolution molecular spin-photon interface at telecommunication wavelengths, *Science*, 2025, **390**, 76–81.

105 (*a*) CCDC 2010809: Experimental Crystal Structure Determination, 2026, DOI: 10.5517/ccdc.csd.cc25hdtx; (*b*) CCDC 2441051: Experimental Crystal Structure Determination, 2026, DOI: 10.5517/ccdc.csd.cc2my3l9.